


ARTICLE

DOI: 10.1038/s41467-018-04603-z

OPEN

Alternative assembly of respiratory complex II connects energy stress to metabolic checkpoints

Ayenachew Bezawork-Geleta^{1,2}, He Wen^{3,4}, LanFeng Dong¹, Bing Yan¹, Jelena Vider¹ ¹, Stepana Boukalova⁵, Linda Krobova⁵, Katerina Vanova⁵, Renata Zobalova⁵, Margarita Sobol⁶, Pavel Hozak⁶, Silvia Magalhaes Novais⁵, Veronika Caisova^{7,8}, Pavel Abaffy⁵, Ravindra Naraine⁵, Ying Pang⁷, Thiri Zaw⁹, Ping Zhang¹, Radek Sindelka⁵, Mikael Kubista^{5,10}, Steven Zuryn², Mark P. Molloy⁹, Michael V. Berridge¹¹, Karel Pacak⁷, Jakub Rohlena⁵, Sunghyoun Park⁴ & Jiri Neuzil^{1,5}

Cell growth and survival depend on a delicate balance between energy production and synthesis of metabolites. Here, we provide evidence that an alternative mitochondrial complex II (CII) assembly, designated as CII_{low}, serves as a checkpoint for metabolite biosynthesis under bioenergetic stress, with cells suppressing their energy utilization by modulating DNA synthesis and cell cycle progression. Depletion of CII_{low} leads to an imbalance in energy utilization and metabolite synthesis, as evidenced by recovery of the de novo pyrimidine pathway and unlocking cell cycle arrest from the S-phase. In vitro experiments are further corroborated by analysis of paraganglioma tissues from patients with sporadic, SDHA and SDHB mutations. These findings suggest that CII_{low} is a core complex inside mitochondria that provides homeostatic control of cellular metabolism depending on the availability of energy.

¹School of Medical Sciences, Griffith University, Southport 4222 Qld, Australia. ²Clem Jones Centre for Ageing Dementia Research, Queensland Brain Institute, University of Queensland, Brisbane 4072 Qld, Australia. ³Department of Biochemistry and Molecular Biology, Shenzhen University School of Medicine, Shenzhen 518060, China. ⁴College of Pharmacy, Natural Product Research Institute, Seoul National University, Seoul 08826, Korea. ⁵Institute of Biotechnology, Czech Academy of Sciences, Prague-West 25250, Czech Republic. ⁶Institute of Molecular Genetics, Czech Academy of Sciences, Prague 14220, Czech Republic. ⁷Eunice Kennedy Shriver National Institute of Child Health and Human Development, National Institutes of Health, Bethesda 20892 MD, USA. ⁸Faculty of Science, University of South Bohemia, Ceske Budejovice 37005, Czech Republic. ⁹Australian Proteome Analysis Facility, Macquarie University, North Ryde 2109 NSW, Australia. ¹⁰TATAA Biocenter, Gothenburg 41103, Sweden. ¹¹Malaghan Institute of Medical Research, Wellington 6242, New Zealand. These authors contributed equally: Ayenachew Bezawork-Geleta, He Wen. Correspondence and requests for materials should be addressed to A.B.-G. (email: a.bezawork-geleta@griffith.edu.au) or to J.R. (email: jakub.rohlena@ibt.cas.cz) or to S.P. (email: psh@snu.ac.kr) or to J.N. (email: j.neuzil@griffith.edu.au)

Mitochondria are semi-autonomous organelles found in the majority of eukaryotic cells. They have their own genome (mitochondrial DNA, mtDNA), which encodes subunits of respiratory complexes and RNA components for mitochondrial protein synthesis. Major roles of mitochondria include generation of energy and synthesis of metabolites. Molecules that are a source of energy are oxidized in a series of biochemical reactions within the tricarboxylic acid (TCA) cycle. Intermediate products of the TCA cycle are used as signaling molecules and as building blocks for various macromolecules, while NADH and FADH₂ are metabolized via oxidative phosphorylation (OXPHOS) to yield ATP. OXPHOS comprises five complexes, CI–CV. CII (succinate dehydrogenase, SDH) contains nuclear-encoded SDHA, SDHB, SDHC, and SDHD subunits, which are recognized as tumor suppressors^{1–3}. Besides its role in OXPHOS, CII converts succinate to fumarate in the TCA cycle, and is thus at the crossroad of the TCA cycle and OXPHOS⁴.

Clinical data document the presence of somatic mutations in mtDNA in cancer in both the regulatory D-LOOP and the coding regions^{5–8}. Previous research has mainly concerned the effects of mtDNA mutations on CI, CIII, CIV, and CV, with CII having been a relatively minor focus. This is explained by the fact that unlike all other OXPHOS complexes, CII does not contain mtDNA-encoded subunits, and therefore no direct effect of mtDNA defects on CII assembly and function has been expected. Further, individual respiratory complexes form supercomplexes (SCs)^{9–11}, while CII acts as a stand-alone complex, with only one report indicating that it can be an SC component¹².

This study investigates whether CII subunits and mtDNA could have any form of interaction in energy production, and if so, whether there is a functional relation that provides an advantage to cells with mtDNA mutations. We show that depletion of mtDNA has an unexpected effect on CII assembly, causing a shift from its tetrameric, fully processed, and assembled form to a slower migrating complex of ~100 kDa, referred to here as complex II_{low} (CII_{low}). Our data suggest that CII_{low} links bioenergetic stress to negative regulation of de novo pyrimidine synthesis and cell cycle progression, which is supported by clinical data from paraganglioma patients with mutations in SDH subunits, indicating that CII_{low} plays an important role in homeostatic control of metabolite synthesis under bioenergetic stress.

Results

mtDNA-linked bioenergetics defects affect the assembly of CII.

Unlike other respiratory complexes, CII is encoded by nuclear DNA and is genetically independent of mtDNA. To understand if mtDNA dysfunction affects CII indirectly, we tested the effect of mtDNA perturbation^{8,13–15} on CII assembly. Native blue gel electrophoresis (NBGE) of mitochondria isolated from murine 4T1 and human MCF7 cells without mtDNA (ρ^0 cells) revealed that CII exists in two hetero-oligomeric forms of ~100 kDa and 124 kDa (migrating on NBGE at ~140 kDa). In 4T1 ρ^0 and MCF7 ρ^0 cells, SDHA was mainly present as CII_{low}, with no known biological function reported to date, and to a lesser degree within fully assembled CII (Fig. 1a). The finding of predominant CII_{low} in 4T1 ρ^0 and MCF7 ρ^0 cells suggests that this form of CII may have a role in (patho)physiological situations where mtDNA is damaged. The size of the processed SDHA protein is ~69 kDa, while CII_{low} migrates on native gels at ~100 kDa. Hence, additional protein components beyond SDHA must be present in CII_{low}.

We next examined CII assembly in human MDA-MB-231 (MDA231) cells. Inhibition of mitochondrial protein synthesis with chloramphenicol (CAB), a blocker of mitochondrial

translation^{16–18}, resulted in depletion of CIII and SCs (Fig. 1b, right panels). Similarly, as with 4T1 ρ^0 and MCF7 ρ^0 cells, CAB-treated MDA231 cells accumulated CII_{low} containing SDHA (Fig. 1b, left panels), suggesting that this form of CII may have (patho)physiological relevance when expression of mtDNA-encoded proteins is compromised.

SDHA is a stable constituent of CII_{low}. To better characterize the subunit composition of CII_{low}, SDHA, SDHB, and SDHC subunits were knocked down one at a time in 4T1 cells using two different siRNAs (siRNA1 and siRNA2), and CII assembly state was followed by NBGE. Depletion of any of the three subunits reduced the level of CII. Interestingly, only the knockdown of SDHA, but not of the other CII subunits, resulted in marked reduction of CII_{low} (Fig. 1c and d), corroborating the presence of SDHA, but not SDHB or SDHC, in CII_{low}.

The identification of SDHA in CII_{low} suggests that it may be more stable than the other CII subunits. We therefore examined the steady state of each subunit in our knockdown cell lines. Depletion of SDHB led to a decrease in the steady state of SDHC, and knockdown of SDHC led to a decrease in the steady state of SDHB. Interestingly, in SDHA knockdown cells, both SDHB and SDHC levels decreased by ~70%. Knocking down either SDHB or SDHC had no effect on the steady state of SDHA (Fig. 1e). It is likely that depletion of SDHA leads to low levels of SDHB and SDHC, probably due to low stability of unassembled subunits as indicated previously^{19–21}.

Characterization of the CII_{low} form of SDH. Based on crystal structure of CII²² (Supplementary Fig. 1a) and our data in Fig. 1e, we hypothesized that depletion of SDHB will result in cells containing only CII_{low}. We thus generated SDHB knockout (KO) MDA231 cells targeting exon 1 (Fig. 2a and b). As with 4T1 cells (Fig. 1c and e), the steady-state level of SDHA was unchanged in SDHB^{KO} MDA231 cells (Fig. 2c). In order to deplete CII_{low}, SDHB^{KO} MDA231 cells were transfected with two different SDHA shRNAs (SDHB^{KO}SDHA^{low-1} and SDHB^{KO}SDHA^{low-2}) and an empty vector (SDHB^{KO}EV) as a control (Fig. 2c; Supplementary Fig. 1b). NBGE analysis showed high levels of CII_{low} in SDHB^{KO} MDA231 cells and little CII_{low} in SDHB^{KO}SDHA^{low} cells (Fig. 2d). We thus prepared models of cells with three variants of CII assembly: fully assembled CII and low levels of CII_{low} (parental cells), cells with only CII_{low} (SDHB^{KO} SDHB^{KO}EV cells), and cells lacking both CII and CII_{low} (SDHB^{KO}SDHA^{low} cells). These models showed low proliferation for both SDHB^{KO} and SDHB^{KO}SDHA^{low} cells (Fig. 2e).

To specify its molecular composition, we transfected SDHB^{KO} cells with SDHA-FLAG and immunoprecipitated the cell-free extract using anti-FLAG IgG. The immunoprecipitate was subjected to tryptic digest followed by MS analysis (Supplementary Fig. 2a), with results of the screen in Supplementary Fig. 2a and Supplementary Data 1. The analysis revealed the presence of the CII assembly factors SDHAF2 (16.7 kDa) and SDHAF4 (9.9 kDa). While SDHAF2 was readily detectable on NBGE membranes in CII_{low} (Supplementary Fig. 2b), the available antibodies did not allow reproducible detection of SDHAF4 after NBGE, and its presence was verified by other means (see below).

We next re-expressed SDHB-FLAG in SDHB^{KO} cells to see whether this would rescue the parental phenotype and whether CII_{low} is reversible. SDHB-reconstituted (SDHB^{rec}) cells were assessed by Western blotting (WB) following SDS-PAGE for the presence of SDHA, SDHB, SDHAF2, and SDHAF4. Supplementary Fig. 2c documents similar levels of SDHA in all three sublines and high levels of SDHB in parental and SDHB^{rec} cells. In contrast, both SDHAF2 and SDHAF4 were low in parental and

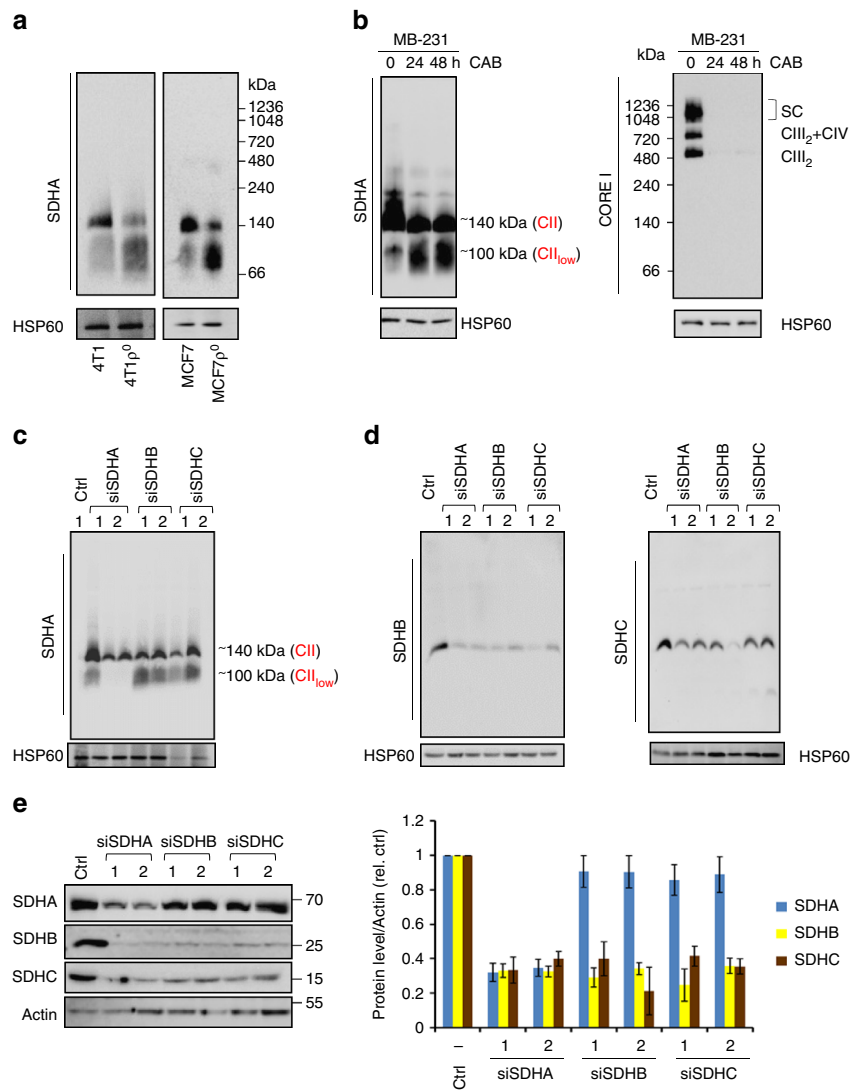


Fig. 1 mtDNA dysfunction affects CII assembly. **a** NBGE analyses of CII assembly from digitonin-solubilized mitochondria isolated from 4T1 and MCF7 cells and their ρ^0 counterparts. **b** NBGE showing formation of CII_{low} and depletion of CIII assembly upon suppression of expression of mtDNA-encoded genes with CAB at indicated time points. **c**, **d** NBGE of CII using mitochondria isolated from 4T1 cells transfected with siRNA against SDHA, SDHB, or SDHC. **e** WB after SDS-PAGE of steady-state levels of CII subunits in 4T1 cells treated with siRNAs as shown (left panel). Right panel shows quantification of WB in the left panel related to actin. The numbers '1' and '2' in **c-e** refer to two different siRNAs. Data shown are mean values \pm SD; images are representative of three independent experiments

SDHB^{rec} cells, but accumulated in SDHB^{KO} cells. We then tested the three sublines by NBGE followed by WB using anti-SDHA IgG and anti-SDHAF2 IgG. Supplementary Fig. 2d reveals that mature CII is re-assembled and the amount of CII_{low} reverts to parental levels in SDHB^{rec} cells, indicating SDHB-dependent reversibility of alternatively assembled CII. Furthermore, SDHAF2 and SDHAF4 were detectable only in SDHB^{KO} cells that lack mature CII but feature CII_{low} , supporting the presence of these assembly factors in CII_{low} cells.

To verify the reversibility of CII_{low} in response to stress, we treated parental cells with CAB for 48 h, followed by 24 h recovery. The amount of CII_{low} was evaluated by NBGE using antibodies against SDHA and SDHAF2, two CII_{low} components readily detectable in this assay (Supplementary Fig. 2e). Treatment with CAB increased the level of CII_{low} , which reverted to baseline within 24 h of treatment cessation. Together with the SDHB^{rec} data, this indicates reversibility of CII_{low} assembly, providing flexibility in response to mitochondrial bioenergetic stress.

CII_{low} does not modulate mitochondrial bioenergetics. We asked whether altered assembly of SDHA affects mitochondrial bioenergetics as well as expression and assembly of other mitochondrial complexes. We found that basal respiration, maximum respiratory capacity, and ATP production were decreased both in SDHB^{KO}EV and SDHB^{KO}SDHA^{low} cells (Fig. 3a-e). Unlike parental cells, absence of spare respiratory capacity and low ATP production were found in SDHB^{KO}EV and SDHB^{KO}SDHA^{low} cells (Fig. 3d, e), further indicating a state of bioenergetic stress. We next assessed oxygen consumption in permeabilized MDA231 cells by high-resolution respirometry. This showed that alteration of the CII assembly status resulted not only in complete suppression of CII-dependent respiration, but also considerably altered CI-dependent respiration (Fig. 3f). Consistent with the above results, we found that assembly of SCs was reduced in SDHB^{KO} and SDHB^{KO}SDHA^{low} cells (Fig. 3g). This is further supported by lower steady-state levels of CI subunits but not CIII, CIV, and CV subunits (Fig. 3h). However, there was no significant difference between SDHB^{KO} and SDHB^{KO}SDHA^{low} cells

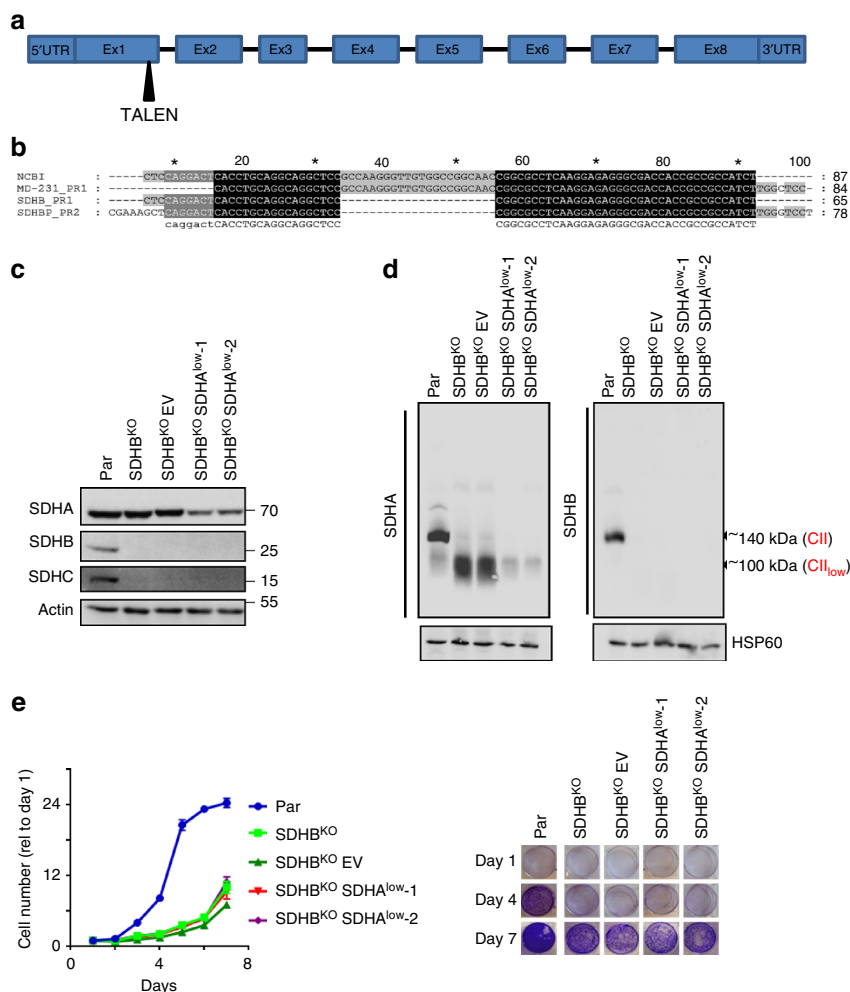


Fig. 2 SDHB depletion stabilizes CII_{low} . **a** A scheme showing the structure of the *SDHB* gene and exon1 as the TALEN target. **b** DNA sequence alignment of the *SDHB* exon 1 from the GenBank nucleotide sequence database, and parental and *SDHB*^{KO} MDA231 cells. Sanger sequencing was done from the PCR product amplified using two pairs of primers (PR1 and PR2) using genomic DNA as a template. **c** WB after SDS-PAGE of CII subunits in individual sublines, as shown. *SDHB*^{KO}EV cells are *SDHB*^{KO} cells transfected with empty vector and were used as a control for stable shRNA transfections. **d** NBGE of mitochondria isolated from parental, *SDHB*^{KO}, *SDHB*^{KO}EV, and *SDHB*^{KO}*SDHA*^{low-1} cells showing three variants of SDHA, using anti-SDHA IgG and anti-SDHB IgG. **e** Proliferation of MDA231 subline was analyzed at the indicated time points using the crystal violet method. Panel on the right shows crystal violet staining at 1, 4, and 7 days. Data are normalized to day 1. Data shown are mean values \pm SD ($n = 3$); images are representative of three independent experiments

for any of the assessed parameters. In contrast, re-expression of SDHB-FLAG (*SDHB*^{rec} cells) substantially recovered the parental phenotype with respect to routine and CII-dependent respiration (Supplementary Fig. S2f).

Cells with severe defects in OXPHOS rely on glycolysis for ATP production and do not grow in the presence of galactose²³. We tested proliferation of MDA231 sublines in galactose- and glucose-containing media, and found that both *SDHB*^{KO}EV and *SDHB*^{KO}*SDHA*^{low} cells failed to proliferate in galactose-containing medium whereas parental cells proliferated efficiently (Fig. 3i). This is in agreement with previous reports on cells with defects in CI and CII assembly^{23–26}. Again, re-expressed SDHB rescued proliferation in galactose-containing media (Supplementary Fig. 2g).

Similarly, analysis of mitochondrial morphology using transmission electron microscopy (TEM) revealed that both *SDHB*^{KO}EV and *SDHB*^{KO}*SDHA*^{low} cells featured mitochondria with altered structure (Supplementary Fig. 3a), consistent with a previous report²⁷. These changes did not affect the steady-state level of several key proteins associated with mitochondrial maintenance and biogenesis (Supplementary Fig. 3b). Thus,

while CII assembly status affected whole-cell bioenergetics and proliferation, CII_{low} had little additional effect on mitochondrial bioenergetics and biogenesis.

Pyrimidine synthesis is attenuated in the presence of CII_{low} .

Having found no direct effect on bioenergetics, we reasoned that CII_{low} could modulate adaptation to altered bioenergetic conditions. Thus, we first performed quantitative proteomic analysis in MDA231 sublines using SWATH-MS²⁸ that resulted in identification and quantification of 1699 individual proteins (Supplementary Data 2). The most downregulated pathway in *SDHB*^{KO}EV cells compared to parental cells was de novo pyrimidine synthesis (Fig. 4a). Quantification of the SWATH-MS data revealed that this downregulation is reversed in *SDHB*^{KO}*SDHA*^{low} cells (Supplementary Fig. 4), indicating that *SDHB*^{KO} cells may suppress anabolic processes to reduce the energy demand, and this is then relieved in *SDHB*^{KO}*SDHA*^{low} cells. To further investigate this issue, we subjected parental, *SDHB*^{KO}, and *SDHB*^{KO}*SDHA*^{low} cells to RNAseq analysis (Supplementary Fig. 5a and b), which revealed significant clusters

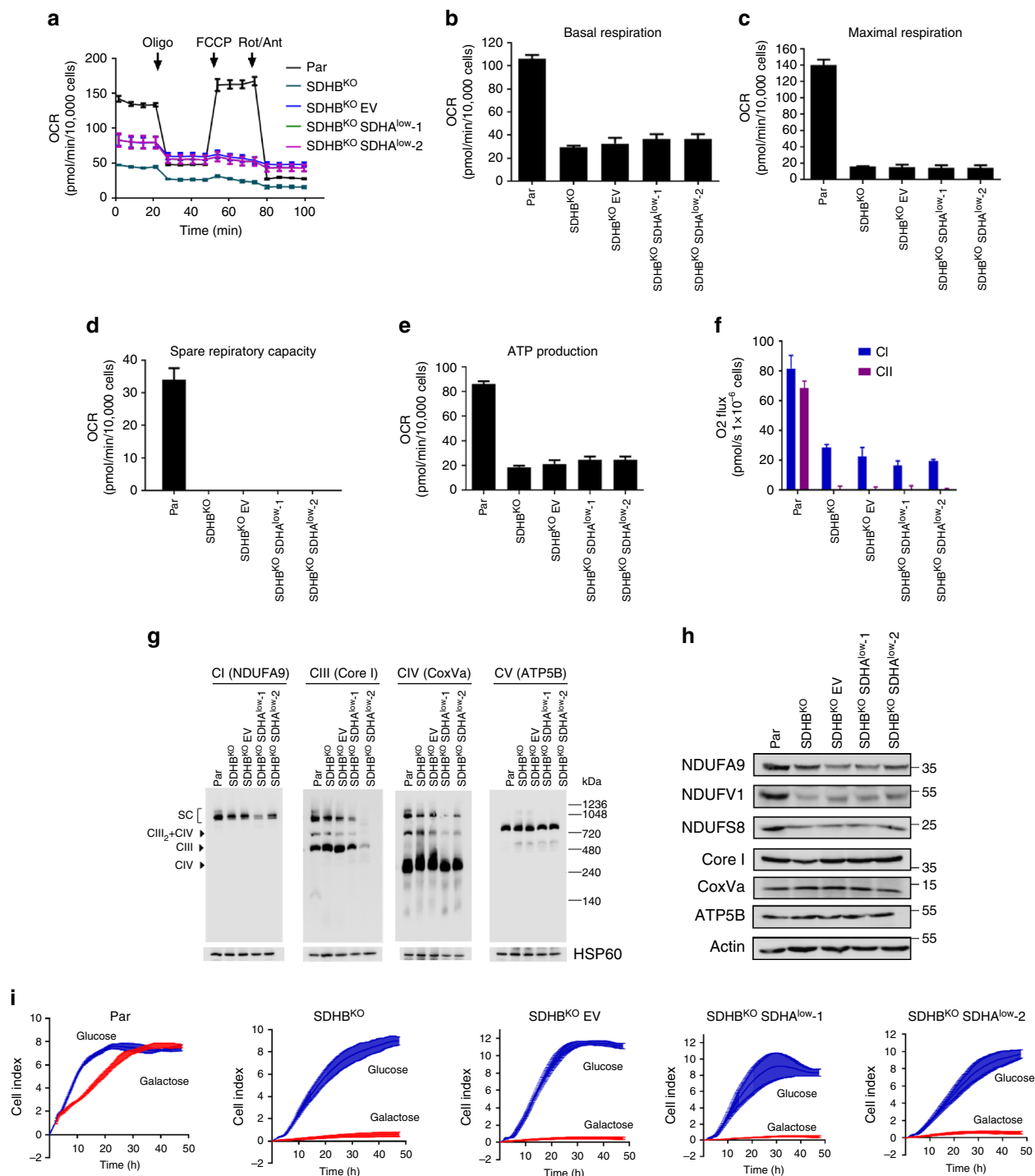


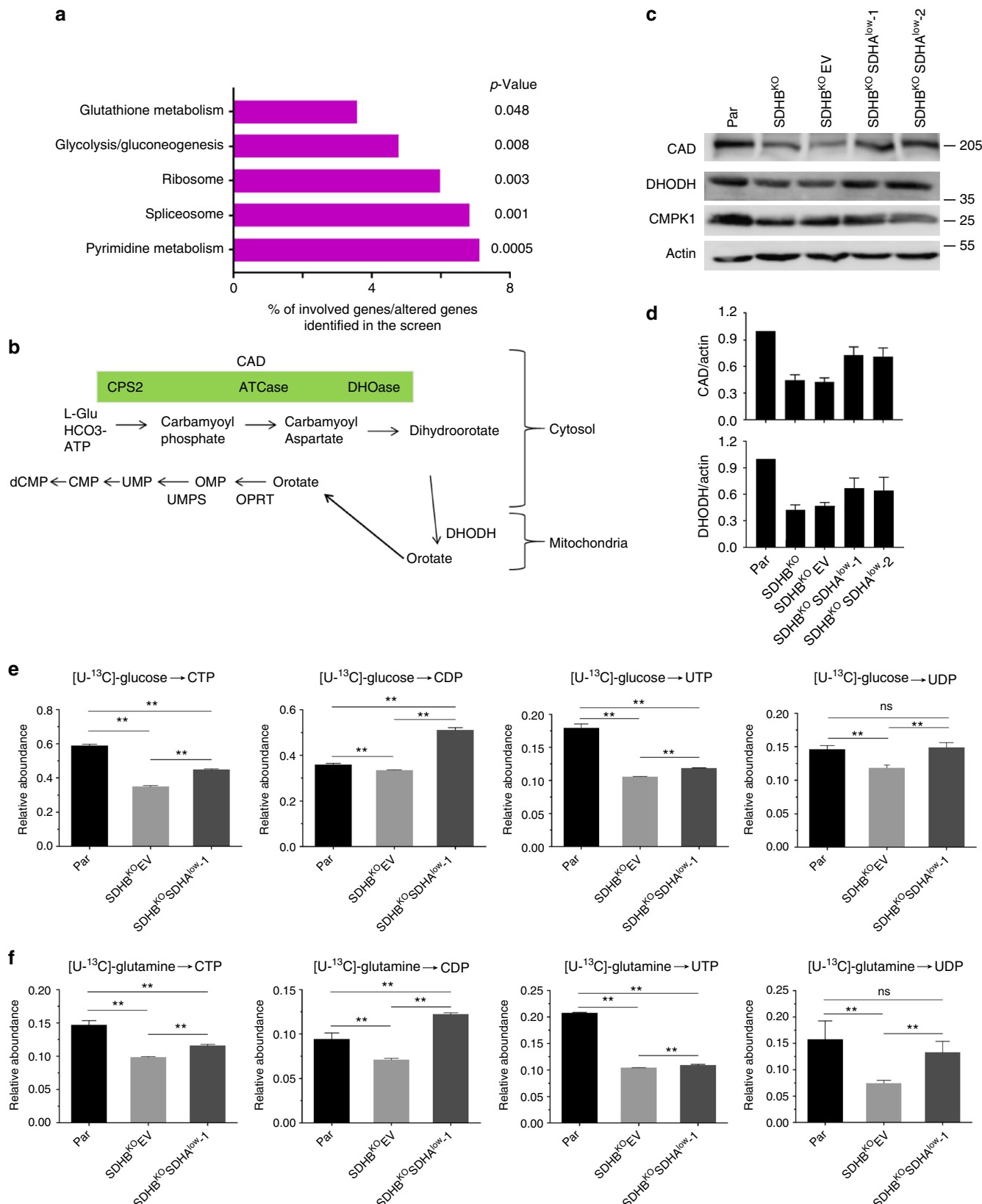
Fig. 3 CII_{low} does not regulate mitochondrial bioenergetics. **a** Oxygen consumption rate (OCR) in MDA231 sublines was followed during sequential additions of oligomycin, FCCP, and combination with rotenone and antimycin. **b–e** Basal respiration, maximal respiration, spare respiratory capacity, and ATP production. **f** CI- and CII-dependent respiration was evaluated in permeabilized cells using the Oxygraph. **g** Mitochondria isolated from MDA231 sublines were subjected to NBGE followed by WB analysis using antibodies against NDUFA9, NDUFV1, NDUFS8 (CI), Core I (CIII), and COXVa (CIV) and ATP5B (CV). **h** MDA231 sublines were analyzed for subunits of OXOPHOS complexes using WB after SDS-PAGE. **i** MDA231 sublines grown in media containing either glucose or galactose were evaluated for proliferation using the xCELLing instrument. Data shown are mean values ± SD (n = 3); images and graphs in **i** are representative of three independent experiments

of genes either upregulated or downregulated in SDHB^{KO} cells with expression being reverted toward parental cell levels in SDHB^{KO}SDHA^{low} cells (Groups 1 and 2 in Supplementary Fig. 5b–f). Gene set enrichment analysis revealed the presence of catabolism-related processes in these clusters, including heterocycle catabolic process (GO:0046700), aromatic compound

catabolic process (GO:0019439), organic cyclic compound catabolic process (GO:1901361), and cellular macromolecule catabolic process (GO:0044265) that were all downregulated in SDHB^{KO}SDHA^{low} cells compared to SDHB^{KO} cells (Supplementary Fig. 5e and f). However, the de novo pyrimidine synthesis pathway did not show significant enrichment, pointing

to modest correlation of transcriptomic and proteomic data as previously reported^{29–33}. Collectively, these data suggest that SDHB^{KO} cells may upregulate catabolic and salvage pathways to compensate for defects in pyrimidine biosynthesis.

We next focused our studies on pyrimidine biosynthesis. Initially, we evaluated representative proteins of this pathway using WB, and found that the trifunctional polypeptide CAD (carbamoyl-phosphate synthase 2, aspartate transcarbamylase,



and dihydroorotase) and dihydroorotate dehydrogenase (DHODH) that catalyze the first four steps of de novo pyrimidine synthesis were attenuated in SDHB^{KO}EV but recovered in SDHB^{KO}SDHA^{low} cells (Fig. 4b–d). Re-expression of SDHB in SDHB^{KO} cells also restored CAD and DHODH (Supplementary Fig. 2h).

We then analyzed pyrimidine nucleotide synthesis directly using stable isotope labeling and LC-MS/MS. The data in Fig. 4e and f, and Supplementary Fig. 7, show that biosynthesis of CTP, CDP, UTP, and UDP from major nutrients glucose and glutamine was low in SDHB^{KO}EV cells but reversed variably in SDHB^{KO}SDHA^{low} cells. These results document that compared to the baseline situation (fully assembled CII), formation of CII_{low} is linked to depressed de novo pyrimidine synthesis, which is reversed with its depletion. The data suggest that under low-energy conditions, CII_{low} may activate cellular processes reducing ATP-consuming pathways such as DNA synthesis to maintain energy balance, which is deregulated in SDHB^{KO}SDHA^{low} cells.

CII_{low} plays a role in cell cycle progression. De novo pyrimidine synthesis is essential for maintaining the nucleotide pool for replication of DNA, thereby controlling cell cycle progression^{34–37}. We thus analyzed cell cycle distribution in MDA231 sublines, which showed that SDHB^{KO} and SDHB^{KO}EV cells were arrested in the S-phase. However, SDHB^{KO}SDHA^{low} cells partially recovered from S-phase arrest with cell cycle distribution similar to that of parental cells (Fig. 5a and b). Cell cycle is regulated by cyclins and cyclin-dependent kinases (CDKs). WB confirmed a marked decrease in the level of CDK6 as well as p16, phosphorylated histone H3 (HH3), and cMYC in SDHB^{KO} and SDHB^{KO}SDHA^{low} cells compared to parental cells (Fig. 5c). Interestingly, p18 was downregulated in SDHB^{KO} and SDHB^{KO}EV cells and recovered in SDHB^{KO}SDHA^{low} cells (Fig. 5c), similar to that seen for steady-state levels of CAD and DHODH and for nucleotide synthesis (Fig. 4). Further, we observed near parental levels of pHH3 in SDHB^{rec} cells (Supplementary Fig. 2h). This result suggests that alteration in SDHA assembly status affects de novo pyrimidine synthesis, and consequently cell cycle progression. Our data suggest that under low-energy conditions, the shift of CII to CII_{low} is associated with a switch to bioenergetically less-demanding processes.

CII_{low} supports growth of SDHB-deficient tumors. Figure 2e reveals no difference in proliferation between SDHB^{KO}EV and SDHB^{KO}SDHA^{low} cells, suggesting that CII_{low} is not critical for proliferation under nutrient-rich conditions. However, imbalance of energy production and anabolic metabolism such as that linked to DNA synthesis could be critical for biomass production required for growth and survival under sub-optimal conditions³⁸. To see whether CII_{low} is important for the tumorigenic potential of MDA231 sublines, migration of parental, SDHB^{KO}EV, and SDHB^{KO}SDHA^{low} cells was tested. Contrary to the cell proliferation assay (Fig. 2e), SDHB^{KO}SDHA^{low} cells showed a lower rate of migration from serum-free media compared to both parental and SDHB^{KO}EV cells (Fig. 5d). To extend these results

to a pathologically relevant situation, we tested the capacity of the sublines to form tumors. Parental, SDHB^{KO}EV, and SDHB^{KO}SDHA^{low} cells were grafted subcutaneously into Balb-c nu/nu mice, and tumor progression was analyzed by ultrasound imaging (USI). Compared to parental cells, SDHB^{KO}EV cells formed tumors with a delay of about 15 days and at lower rate, while SDHB^{KO}SDHA^{low} cells failed to form tumors 60 days post grafting (Fig. 5e and f). To understand whether the inability of SDHB^{KO}SDHA^{low} cells to form tumors is linked to their higher vulnerability under nutrient-poor conditions, we evaluated the level of cell death in individual sublines grown in galactose media. Supplementary Fig. 3c, d shows that all sublines are mostly viable in glucose-containing media, while SDHB^{KO}SDHA^{low} cells are more vulnerable to cell death than SDHB^{KO} cells in non-permissive, galactose-containing media. These data point to a link between CII_{low} and energy balance regulation to maintain cellular fitness under nutrient-poor conditions.

CII_{low} modulates the metabolome. In order to better understand metabolic consequences of alternative SDHA assembly, we examined the metabolic profiles of MDA231 sublines. Metabolomic data obtained by one-dimensional (1D) nuclear magnetic resonance (NMR) were combined with additional 16 metabolites, measured using targeted LC-MS/MS that are important in central energy metabolism but are not readily quantifiable by NMR (Supplementary Data 3). Results of this analysis, represented by the heat map in Fig. 6a, indicate an effect of CII_{low} on the differential metabolite profile in MDA231 sublines. The data show that the metabolic profile of SDHB^{KO}EV cells has very little overlap with that of the parental cells, whereas SDHB^{KO}SDHA^{low} cells have significantly more overlap. This is consistent with partial least square discriminant analysis (PLS-DA) of the metabolomic data showing the metabolic differences between sublines and the closer position of the SDHB^{KO}SDHA^{low} cells to parental cells along the PLS1 axis (Fig. 6b). Taken together with the results in Fig. 1 which demonstrated CII_{low} formation during OXPHOS dysfunction, these data suggest that CII_{low} is linked to metabolic modulation when bioenergetics is compromised.

Depletion of CII_{low} reverses accumulation of succinate. Given the role of SDHA in the TCA cycle, we expect that CII_{low} could affect succinate metabolism and TCA cycle activity. We therefore subjected parental, SDHB^{KO}EV, and SDHB^{KO}SDHA^{low} cells to two-dimensional (2D) in-cell NMR analysis, which allows monitoring of metabolites in live cells in real time³⁹. The approach detects metabolite levels as a function of time, as opposed to steady-state levels at a single time-point as reported above and in most metabolomics studies. This facilitates estimation of actual activities of metabolic pathways leading to particular metabolites in live cells. Thus, cells were incubated with [U-¹³C]glucose, and production of ¹³C isotope-containing pyruvate, lactate, alanine, and the TCA cycle intermediate succinate was monitored. As expected, parental cells differed in all assessed metabolites from the two sublines. SDHB^{KO}EV cells showed increased intracellular levels of lactate and alanine compared to SDHB^{KO}SDHA^{low} cells,

Fig. 4 Pyrimidine biosynthesis is suppressed in the presence of CII_{low}. **a** Label-free quantitative proteomic analysis of downregulated proteins in SDHB^{KO} MDAMB231 cells and the percentage of proteins identified per pathway relative to genes with significantly altered expression in SDHB^{KO} cells. **b** Scheme of the de novo pyrimidine nucleotide synthesis pathway. **c** SDS-PAGE following WB analysis of MDA231 sublines for proteins of the de novo pyrimidine pathway. **d** Densitometric evaluation of the level of the CAD and DHODH proteins by WB. Relative isotopomer amounts (M+1) of CTP, CDP, UTP, and UDP were assessed by LC-MS/MS using [U-¹³C] glucose (**e**) and [U-¹³C] glutamine (**f**) as tracers. Data shown are mean values ± SD (n ≥ 3); images are representative of at least three independent experiments. The symbol ** indicates differences with p < 0.05 and 'ns' indicates non-significant differences, as assessed by the two-tailed unpaired Student's t-test

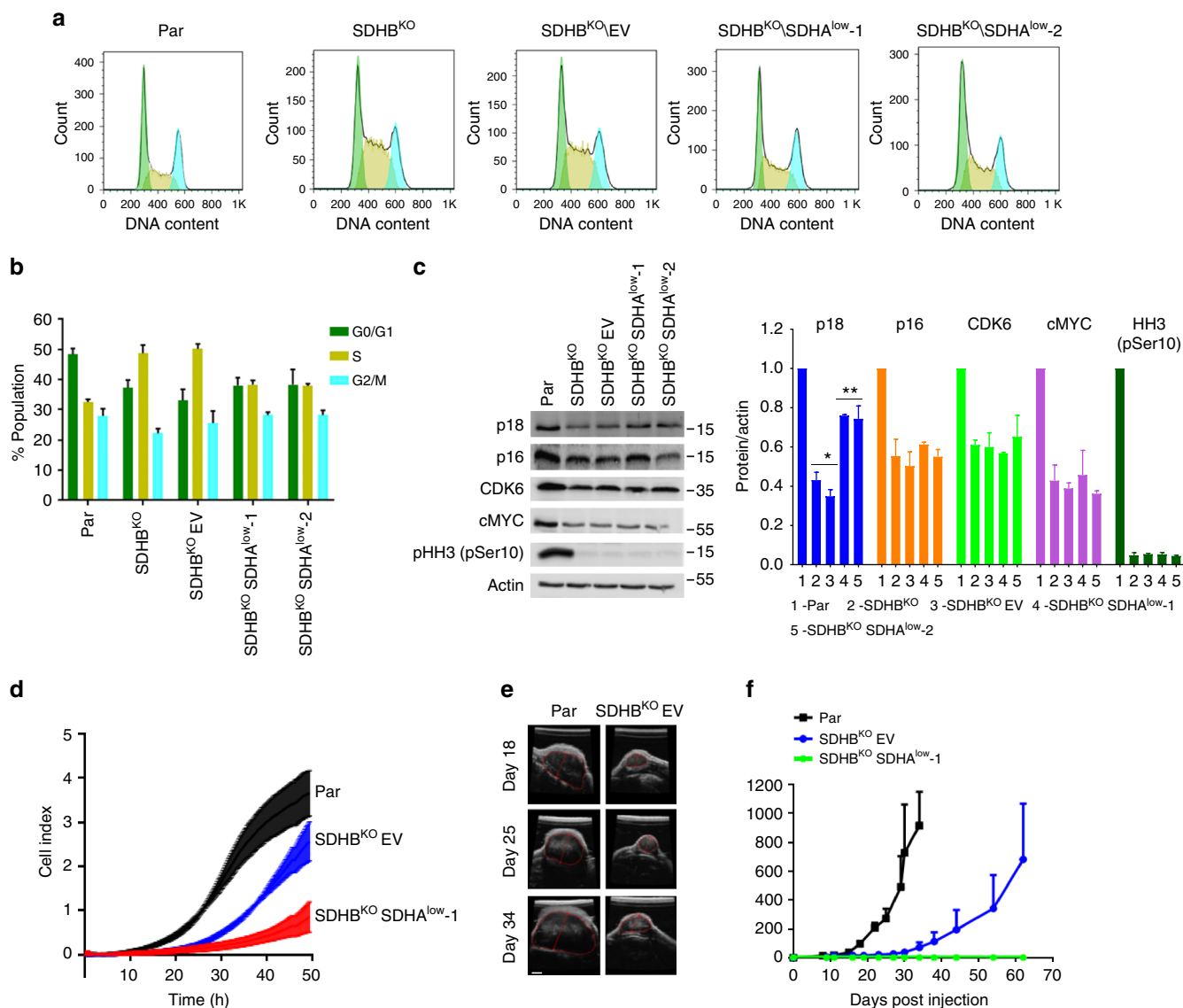


Fig. 5 CII_{low} supports growth of SDHB-deficient tumors. **a** MDA231 sublines were evaluated for cell cycle distribution using flow cytometry and staining with propidium iodide. Green color indicates cells in G0/G1 phase, yellow cells in S phase, and blue color cells in G2/M phase. **b** Histograms show evaluation of data in panel (a) representing 10^4 cells. **c** SDS-PAGE followed by WB analysis of proteins linked to the regulation of cell cycle progression and mitosis; images are representative of three independent experiments. **d** MDA231 sublines were assessed for migration capacity using the xCELLigence system. **e** MDA231 sublines were grafted in Balb-c nu/nu mice at 10^6 cells per animal, and tumor progression was visualized and quantified by ultrasound imaging. The bar represents the size of 2 mm. **f** Representative images of tumors derived from parental and SDHB^{KO} EV cells. Data shown are mean values \pm SD ($n = 5$ for **b** and **c**). The symbol * indicates significant differences compared to parental cells with $p < 0.05$ and ** significant differences compared to SDHB^{KO} cells with $p < 0.05$, as assessed by the two-tailed unpaired Student's *t*-test

while fatty acid synthesis was not altered (Fig. 6c). Therefore, reduction of CII_{low} in SDHB^{KO}SDHA^{low} cells seems to induce shuttling of pyruvate to pathways other than glycolysis without affecting fatty acid metabolism. Importantly, SDHB^{KO}EV cells had a higher level of succinate than parental cells, in agreement with previous reports for other SDHB^{KO} models^{40–44}. However, SDHB^{KO}SDHA^{low} cells showed reduced succinate levels compared to SDHB^{KO}EV cells (Fig. 6c), suggesting a CII_{low} -dependent change in succinate metabolism, which may be due to activation of an alternative metabolic route of succinate utilization.

CII_{low} negatively regulates anabolic activity of TCA cycle. To obtain further insight into succinate metabolism as well as

metabolism of other TCA cycle intermediates, we monitored the fate of [U-¹³C] glucose and [U-¹³C] glutamine in MDA231 sublines using LC-MS. The first cycle of TCA metabolism of [U-¹³C] glucose via acetyl-CoA will generate four-carbon metabolites with two ¹³C nuclei (m+2 isotopomer) through oxidative decarboxylation (Fig. 7a–f). Alternatively, an m+3 isotopomer can be formed if glucose enters the TCA cycle via the pyruvate carboxylase (PC) pathway (Fig. 7a). In agreement with the above NMR data (Fig. 6c), we observed increased m+2 isotopomers of succinate in SDHB^{KO}EV cells, and this was reduced in SDHB^{KO}SDHA^{low} cells (Fig. 7d). Concurrently, the levels of m+2 isotopomers of aspartate, malate, and fumarate increased in SDHB^{KO}SDHA^{low} cells compared to SDHB^{KO}EV cells (cf. Fig. 7e–g), suggesting more efficient consumption of succinate in cells with lower levels of CII_{low} . The increase in m+3

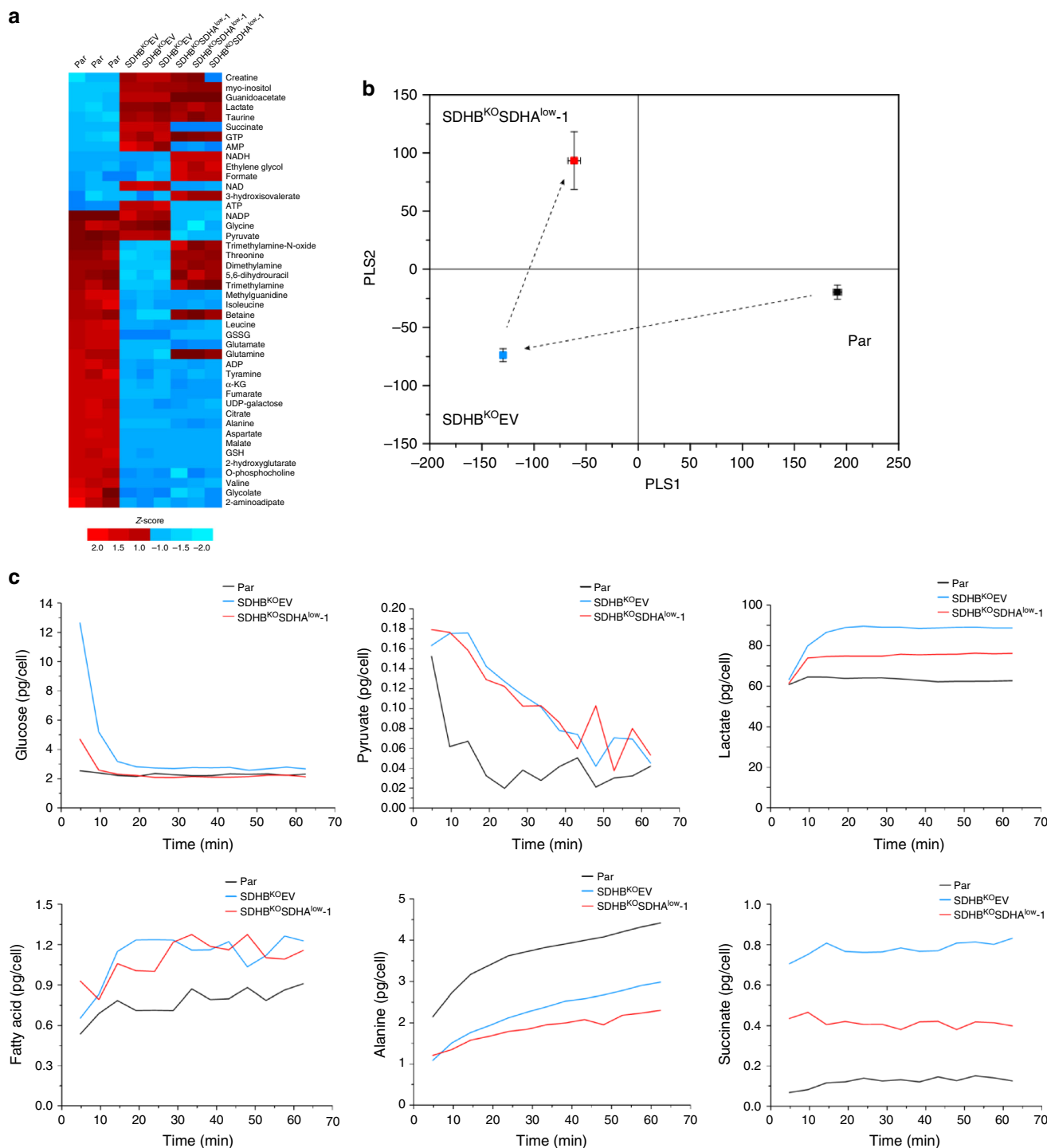


Fig. 6 Cl_{low} modulates metabolome of MDA231 sublines. **a** The heat map was constructed with the Z-score of peak intensities of each metabolite identified by both 1D NMR and LC-MS/MS from parental, SDHB^{KO}EV, and SDHB^{KO}SDHA^{low} cells. The Z-score was obtained by dividing the difference between actual peak intensities and mean value by the standard deviation. **b** Score plot from partial least squares discriminant analysis (PLS-DA) on MDA231 sublines with the entire 1D NMR spectral data. PLS1 axis accounts for the major metabolic discrimination (63.5%), and the PLS2 16.8%. The symbols represent the mean score values from the multivariate analysis and the whiskers represent one standard deviation. Transitions are shown by arrows. **c** Real-time flux comparison in live parental, SDHB^{KO}EV, and SDHB^{KO}SDHA^{low} cells. Time-dependent metabolic changes were obtained using 2D in-cell NMR metabolomics approach. The absolute quantification is based on the level of ¹³C carbon on a particular atom of metabolites detectable by NMR and was performed as described previously³⁹. Although it is not possible to differentiate pre-existing natural abundance metabolites with those derived from ¹³C-glucose with real-time NMR, the natural abundance of ¹³C is 1% and pre-existing metabolites should not make significant contributions to the quantitation. Fatty acid represents the aggregate level of the ¹³C-labeled CH₂ peak from free fatty acids at 1.36 and 32.0 ppm on the HSQC spectrum. Parental, black; SDHB^{KO}EV, blue; SDHB^{KO}SDHA^{low}, red

isotopomer of aspartate and malate in SDHB^{KO}SDHA^{low} cells, but not that of fumarate (Fig. 7e–g), suggests that the PC pathway may also contribute to the four-carbon metabolites in these cells.

[U-¹³C] glutamine feeds carbons into the TCA cycle via α-ketoglutarate. A subsequent oxidative decarboxylation in the TCA cycle generates the m+4 isotopomer of succinate that can lead to m+4 aspartate (Fig. 7h, j–n). Succinate and aspartate m+2

isotopomers can also be formed through the TCA cycle if the m+4 succinate condenses with acetyl-CoA, followed by oxidative decarboxylation in subsequent TCA cycles (Fig. 7h, green). [U-¹³C] glutamine can also contribute to formation of the m+3 isotopomer of aspartate via reductive carboxylation (Fig. 7h, red). In parental cell lines, we observed simultaneous oxidative decarboxylation and reductive carboxylation of glutamine as

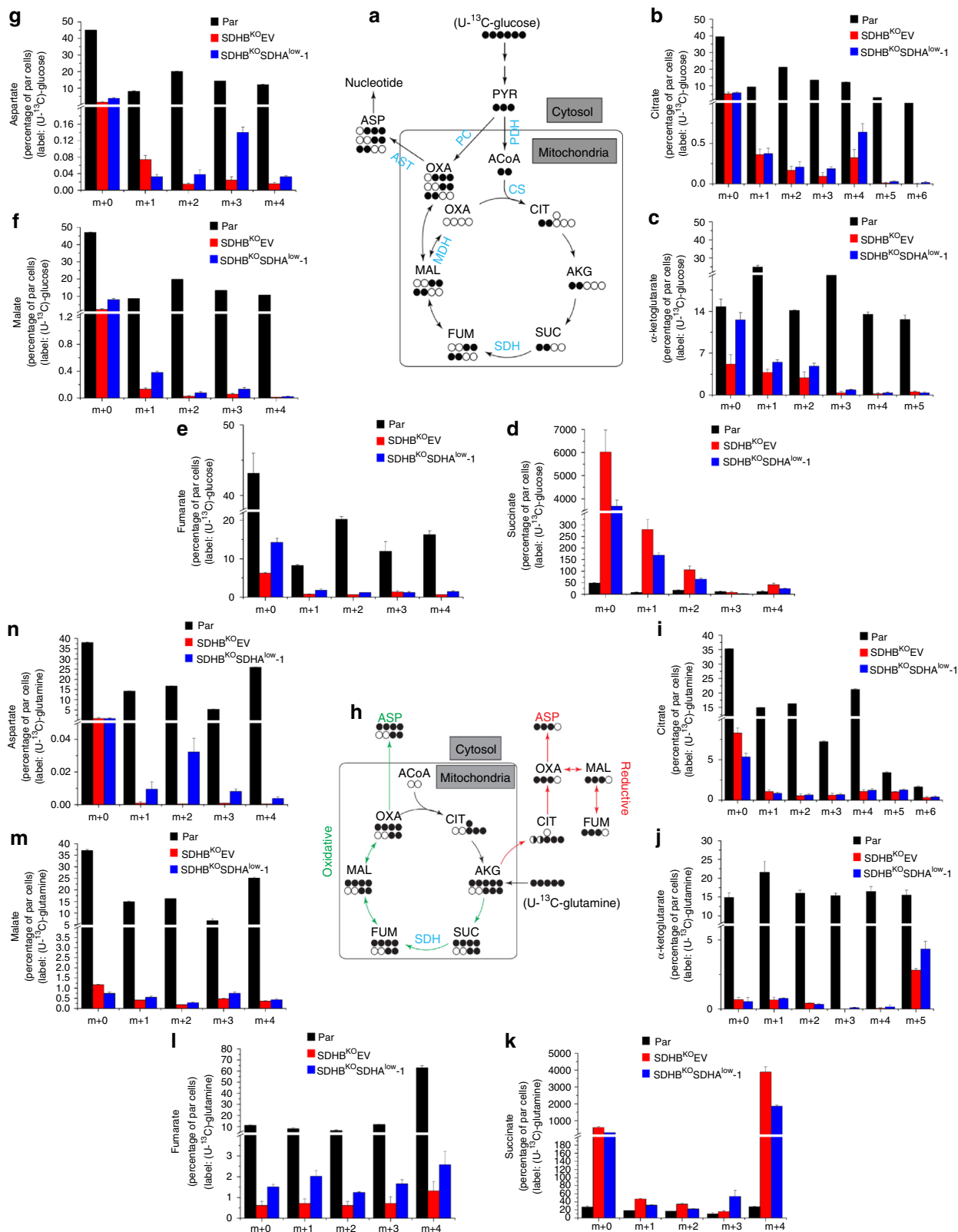


Fig. 7 CII_{low} restricts TCA-linked anabolism. **a** and **h**, Predicted labeling patterns of indicated metabolites from U-¹³C₆-glucose (**a**) and from U-¹³C-glutamine (**h**) (filled circles ¹³C; open circles ¹²C). The oxidative (green) and reductive (red) carboxylation pathways are indicated (**h**). Isotopologue distribution of intracellular citrate (**b, i**), α-ketoglutarate (**c, j**), succinate (**d, k**), fumarate (**e, l**), malate (**f, m**), and aspartate (**g, n**) after incubation for 24 h with 5 mM unlabeled glucose and 20 mM U-¹³C-glucose or 4 mM U-¹³C-glutamine, respectively. The data were obtained using LC-MS/MS analysis. The Y values are presented as the percent values of the sum of all the isotopologues per each metabolite in parental cells; 'm + ...' indicates the relevant isotopomer. Data are presented as mean ± SD, n = 3. PYR pyruvate, ACoA acetyl-CoA, CIT citrate, AKG α-ketoglutarate, SUC succinate, FUM fumarate, MAL malate, OXA oxaloacetate, ASP aspartate, PDH pyruvate dehydrogenase, PCX pyruvate carboxylase, CS citrate synthase, SDH succinate dehydrogenase, MDH malate dehydrogenase, AST aspartate transaminase

shown by high levels of incorporation of [U-¹³C] glutamine into m+2, m+3, and m+4 aspartate isotopomers (Fig. 7n), consistent with reports on other cancer cells^{45–48}. Significant formation of m+5 citrate isotopomer also suggests reductive carboxylation in parental cells (Fig. 7i). We observed very high absolute incorporation of [U-¹³C] glutamine into m+4 succinate in SDHB^{KO}EV and a significant decrease to about half in SDHB^{KO}SDHA^{low} cells (Fig. 7k). These were accompanied by higher incorporation of [U-¹³C] glutamine into m+4 aspartate and fumarate in SDHB^{KO}SDHA^{low} cells than SDHB^{KO}EV cells (Fig. 7l and n). Similar patterns were observed for the m+2 succinate isotopomer (Fig. 7k), although the absolute incorporation was much lower, probably due to a second round of the TCA cycle. These glutamine incorporation data clearly indicate that glutamine-derived succinate accumulates in SDHB^{KO}EV cells, whereas it is converted to fumarate and ultimately to aspartate more efficiently in SDHB^{KO}SDHA^{low} cells.

Overall, both glucose and glutamine isotope incorporation experiments indicate a block in succinate metabolism in SDHB^{KO}EV cells that is at least partially lifted when the CII_{low} is depleted on the SDHB^{KO} background (Supplementary Fig. 5a and c). This phenomenon is also consistent with the reverse trend of fumarate, whose level increased in SDHB^{KO}SDHA^{low} cells (Supplementary Fig. 5b and d). This re-flow of succinate is suggested to induce redistribution of carbon atoms of glucose and glutamine to four-carbon metabolites leading to the recovery of synthesis of aspartate, a precursor for pyrimidine synthesis.

Previous studies showed that CII dysfunction caused by SDHB–SDHD mutations/deficiency results in accumulation of succinate^{2,40,42–44,49,50}. Here we demonstrate that SDHA maintains high levels of succinate following CII dysfunction. Our data also implicate a switch of carbon metabolism in a CII_{low}-dependent manner, mainly from succinate accumulation to anabolic reactions, including synthesis of aspartate to produce pyrimidines. Further investigations are needed to elucidate the enzymatic activity of CII_{low}, especially in the context of succinate accumulation due to reductive carboxylation of glutamine (Fig. 7h).

CII_{low} is a feature of SDHB-deficient paraganglioma. To assess the clinical relevance of our findings, we inspected tumor tissue from paraganglioma patients with SDHA and SDHB mutations, as well as sporadic paraganglioma patients. We assessed tumors from six patients for the presence of SDHA and SDHB using immunohistochemistry. Fig. 8a shows that samples from patients with mutated SDHB exhibit high levels of SDHA, while tumor tissue derived from a patient with SDHA mutation showed very low levels of both SDHA and SDHB proteins. Next, tumors of these patients were evaluated for CII assembly and for the level of de novo pyrimidine synthesis. The rate-limiting trifunctional CAD protein as well as cell cycle regulatory proteins were assessed. NBGE showed high levels of CII_{low} and low levels of fully assembled CII in tumors with SDHB mutations, while tumors with SDHA mutations showed low levels of fully assembled CII and the absence of CII_{low} (Fig. 8b). Further, SDHA-

mutated paragangliomas lacked FAD, a cofactor of CII associated with the catalytic subunit SDHA, while it was detected in sporadic paragangliomas or those with SDHB mutations. Paragangliomas with high levels of CII_{low} were found to contain low levels of CAD and p18 (Fig. 8c and d). These data are in agreement with results found for sublines of MDA231 cells with different CII assembly status (Fig. 2d; Fig. 4c; Fig. 5c). The data imply that CII_{low} may vary under different (patho)physiological conditions, giving our findings clinical relevance.

Discussion

In the present study, we show that alternative assembly of CII fine-tunes cellular metabolic homeostasis to compensate for chronic bioenergetic stress. SDHA is known to exist in a complex with other subunits of CII, with an overall molar mass of 124 kDa, migrating on native gels at ~140 kDa^{22,51}. We found an assembly form of SDHA migrating at ~100 kDa (designated here as CII_{low}; Figs. 1 and 2), lacking SDHB and SDHC. This is consistent with previous studies using an experimental model of yeast, mammalian cell culture, and human pathological conditions showing that SDHA is stable in the absence of SDHB^{40–44,52}, although its biological function has never been investigated. In addition, CII_{low} is more prevalent when mtDNA is depleted or its expression is compromised (Fig. 1). This suggests biological relevance of CII_{low} with mtDNA mutations and under conditions that limit mitochondrial energy production. We propose that CII/CII_{low} has a role in mitochondria similar to that of pyruvate kinase 2 (PKM2), which changes its assembly from a highly active tetrameric to low-active dimeric form in response to different cellular signaling pathways. A switch from the tetrameric to dimeric form of PKM2 has profound consequences for cellular metabolism as well as proliferation in the context of diabetic nephropathy⁵³ and tumorigenic capacity of cancer cells^{54–56}.

The molecular weight of SDHA is about 70 kDa and thus there are likely to be other SDHA-interacting proteins in CII_{low} of approximately 100 kDa. To identify SDHA-interacting proteins, we used immunoprecipitation followed by MS analysis. This analysis, supported by WB, identified the assembly factors SDHAF2 and SDHAF4 as proteins that together with SDHA constitute CII_{low} accounting for its ~100 kDa mass (Supplementary Fig. 2). We have recently reported that SDHAF2 has redundant function in relation to CII activity in MDA231 cells⁵⁷. While we do not know the function of SDHAF2 and SDHAF4 in CII_{low}, it is possible that these factors form a functional association with SDHA within CII_{low} and in the absence of the other three subunits (SDHB–D). The role of SDHAF2 and SDHAF4 in CII_{low} is the subject of current investigation.

To study the cellular function of CII_{low}, we established stable cellular models with three different assembly forms of SDHA (Fig. 2) and initially analyzed bioenergetics difference of these sublines. We found that SDHB^{KO} cells with prominent presence of CII_{low} switched to low basal respiration with no spare respiratory capacity, indicating an energy stress situation. SDHB^{KO}SDHA^{low} cells with depleted CII_{low} showed a bioenergetic pattern similar to that of SDHB^{KO} cells (Fig. 3), indicating

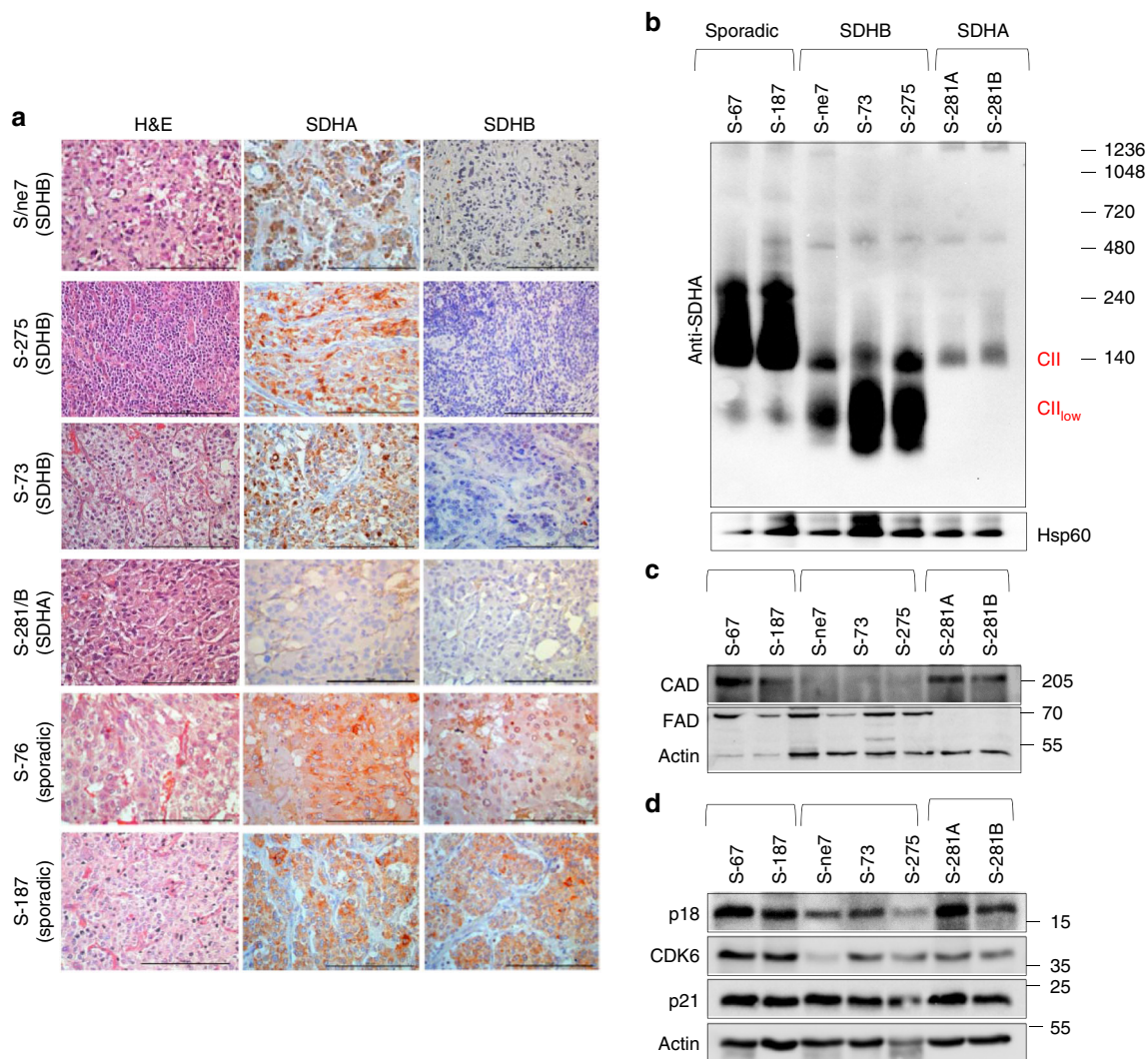


Fig. 8 CII assembly and de novo pyrimidine pathway in paragangliomas. **a** Histological examination of SDHA and SDHB expression from tumor tissue of paraganglioma patients with *SDHA* or *SDHB* mutations or with sporadic paragangliomas. Tissues were processed for H&E staining and immunohistochemistry using SDHA and SDHB IgGs. Representative images are collected using a 40× objective. Scale bars represent 100 μm. **b–d** Paraganglioma tissues, as shown, were assessed by WB following protein separation by NBGE for CII assembly using anti-SDHA IgG (**b**), and by SDS-PAGE for CAD and FAD (**c**) and for markers of cell cycle (**d**). Images are representative of three independent experiments

that CII_{low} plays only a minimal role in mitochondrial bioenergetics.

Label-free proteomic and pathway analysis allowed for identification of differences in the de novo pyrimidine pathway in MDA231 sublines. We found that CII_{low} abundance is inversely correlated with de novo pyrimidine pathway activity (Fig. 4), as exemplified by the steady-state level of CAD, a trifunctional and rate-limiting polypeptide in the pathway. The level of the CAD protein was reduced by approximately 60% in SDHB^{KO} cells resulting in cell cycle arrest in the S-phase, and its re-expression in SDHB^{KO}SDHA^{low} cells with depleted CII_{low} normalized cell cycle progression (Fig. 5). Recently, the de novo pyrimidine synthesis pathway has been shown to be essential in metabolic rewiring that modulates chemotherapy resistance of triple-negative breast cancer⁵⁸ and other neoplastic pathologies^{59,60}, supporting the notion that de novo pyrimidine synthesis improves plasticity of cancer cells at the expense of increased energy consumption. Further investigations will be needed to provide unequivocal evidence for a functional linkage between CII_{low} and pyrimidine biosynthesis. However, our data suggest that CII_{low} exerts its protective function not by modulating

mitochondrial bioenergetics (i.e., OXPHOS), but through other mitochondria-related mechanisms, which are not yet fully defined but seem to involve energy conservation strategies such as a reduction of the de novo pyrimidine synthesis pathway. Therefore, we propose that restriction of this pathway and possibly of other energy-demanding processes by CII_{low} may provide a selective advantage under suboptimal nutrient conditions when bioenergetics is compromised, exemplified by increased cell death in galactose media and a the failure to form tumors in a mouse xenograft model (Fig. 5) when SDHB-deficient cells lose CII_{low}. In line with this, CII_{low} is less abundant in optimal physiological conditions and becomes the dominant SDHA form of CII during sub-optimal energy production (Fig. 1).

Our data suggest that deficiency of CII assembly and the shift of SDHA to CII_{low} modulates metabolism in response to compromised mitochondrial bioenergetics. It introduces checkpoints of cellular functions with high demands for energy, for example reducing formation of aspartate that is essential for pyrimidine nucleotide synthesis. This indicates that CII_{low} might be a sensor of bioenergetic stress, providing a feedback from OXPHOS to central carbon metabolism. Similarly, a number of proteins

capable of sensing mitochondrial energy production or metabolite levels that reflect energy status have been identified. AMP-activated protein kinase (AMPK) has been shown to sense the ratio of ATP to ADP and AMP level in order to initiate an energy compensating stress response^{61,62}. Previous studies have also demonstrated that certain sirtuins are sensors of organelle energy production in relation to the NADH/NAD⁺ ratio⁶³. Recently the ubiquinol/ubiquinone ratio has been reported to sense mitochondrial energy production linked to the respiratory status⁶⁴. Possible links between CII assembly forms and other sensors of mitochondrial bioenergetic dysfunction need to be further investigated. Merging these various individual components into a highly integrated regulatory system presents the next challenge.

Data shown here reveal that patients with *SDHB* and *SDHA* mutations have different CII assembly status. We found that CII_{low} is the remaining unit of CII present in patients with *SDHB* mutations, but is absent in patients with *SDHA* and sporadic mutations. In agreement with our cellular model of MDA231 sublines, patients that show high levels of CII_{low} also have reduced levels of the de novo pyrimidine synthesis regulatory enzyme CAD and the cell cycle modulator protein p18 (Fig. 8). Clinical data also indicate that *SDHB* mutation-associated paragangliomas are less proliferative but are associated with higher invasiveness and metastasis^{42,65–67}. This may be one of the reasons why *SDHA*-deficient tumors are relatively rare, possibly due to an imbalance in energy and metabolic homeostasis. Thus, our data provide more detailed insights into established clinic-pathological features for incurable *SDHx*-related paragangliomas and may potentially serve as a diagnostic marker.

In summary, we found that following mtDNA depletion or *SDHB* deficiency, an alternative CII with different activity is formed. We suggest that the existence of CII_{low} in patients with *SDHB*-mutated paragangliomas may contribute to a cellular mechanism resulting in severe pathological outcomes, including enhanced migration and invasiveness. Hence, *SDHA* epitomizes a moonlighting protein, being an enzyme that is a baseline tumor suppressor but becomes a promoter of tumor growth in the context of bioenergetic deficiency.

Methods

Cells and transfection. MDA231 and MCF7 cells were obtained from the ATCC and cultured in DMEM (Life Technology) supplemented with 10% FCS and antibiotics plus antimycotics (Gibco). To generate *SDHB*^{KO} cell lines, MDA231 cells were transfected with the TALEN construct obtained from Genecopia. Transfections were performed using Lipofectamine 2000 (Invitrogen) according to the manufacturer's instructions; transfectants were selected with hygromycin. Two shRNAs targeting the human *SDHA* gene and empty vector (EV) were purchased from OriGene. *SDHB*^{KO} cells were transfected with the shRNA plasmids. After 36 h, cells were treated for 5 days with 0.8 µg/ml puromycin. Preparation of mtDNA-depleted cells (4T1p⁰ and MCF7p⁰) was accomplished by their long-term incubation with 50 µM EtBr^{13,57}. Human *SDHB* was re-expressed in *SDHB*^{KO} cells from the pLYSS-*SDHB*-Flag plasmid⁶⁸ (Addgene # 50055, a kind gift of Vamsi Mootha) using lentiviral transduction. Lentivirus particles were produced in Hek293T cells using second generation psPAX and pMD.2G plasmids and lipofection (Lipofectamine 3000, Invitrogen). Virus-containing media were collected after 48 h, centrifuged at 3000×g for 15 min and stored at –80 °C⁶⁹.

Proliferation, migration, and cell death assays. Parental, *SDHB*^{KO}EV, and *SDHB*^{KO}*SDHA*^{low} cells were plated in a 24-well dish in DMEM. At indicated times, cell proliferation was assessed by crystal violet assay using a standard protocol. xCELLigence Real-Time Cellular Analysis system was used to evaluate cell proliferation in glucose- or galactose-containing medium and using dialyzed FBS (Gibco). For this, cells were seeded in 16-well E-plates (4 replications per cell type) as recommended by the manufacturer. For migration assays, cells were transferred to the CIM-16 plates and allowed to migrate toward FBS placed in the other compartment. Cell proliferation was monitored in real time using the xCELLigence instrument for 50 h, and the cell index was recorded every 5 min. Cell death was assessed using the standard annexin V/propidium iodide (PI) method.

siRNA transfections. Mouse Silencer-select pre-designed *SDHA*-, *SDHB*-, and *SDHC*-targeting siRNAs and non-silencing controls were obtained from Life Technologies. The sequences are as follows: *SDHA* target sequence-1 (s84146): GGA ACA CUC CAA AAA CAG Att; *SDHA* target sequence-2 (s211850): CCA GUU AUU UUG UGG AAU Att; *SDHB* target sequence-1 (s205969): GCU UUA AUC AAG AUC AAG Att; *SDHB* target sequence-2 (s205970): CCC UCU UCC ACA UAU GUA Utt; *SDHC* target sequence-1 (s82476): GAU CUA CUC GGC UAA GUU Utt; *SDHC* target sequence-2 (s205071): GAA CAC GAG UUC AAA CCG Utt. 4T1 cells were transiently transfected with 20 nM siRNA using Lipofectamine RNAiMAX transfection reagent (Invitrogen) according to the manufacturer's instructions and harvested for analysis 72 h after transfection.

Cell cycle analysis. Cells were harvested with trypsin, rinsed with PBS, fixed by drop-wise addition into 70% (v/v) ethanol and kept at –20 °C for at least 4 h. They were then centrifuged, rinsed in PBS, re-suspended in PBS containing 80 µg/ml RNase and 30 µg/ml of propidium iodide plus 100 µg/ml RNase A. After incubating for 30 min at room temperature, DNA content was assessed using the FACS Calibur flow cytometer (Becton Dickinson). Cell cycle distribution was estimated using the FlowJo software and the Watson distribution model.

Western blotting. Cells were lysed in 20 mM Tris (pH 8), 200 mM NaCl, 1 mM EDTA, 0.5% (v/v) NP-40, and 10% glycerol supplemented with protease inhibitors (Roche). After addition of the Laemmli solution to the samples, the proteins were separated by SDS-PAGE (8–15% gel) and then transferred to polyvinylidene difluoride (PVDF) membranes. After blocking with 5% non-fat milk, the blots were incubated with the primary antibodies overnight at 4 °C. The membranes were then treated with horseradish peroxidase-conjugated secondary antibodies for 2 h at room temperature, followed by visualization (SuperSignal West Pico Chemiluminescent Substrate, Pierce). The following antibodies were used in the study: *SDHA* (Abcam, ab14715; 1:2000); *SDHB* (Abcam, ab14714; 1:1000); *SDHC* (Abcam, ab155999; 1:1000); HSP60 (Abcam, ab137706; 1:2000; or Cell Signaling, 12165; 1:2000); CoxVa (Abcam, ab110262, 1:2000); NDUFA9 (Life Technologies/Thermo Fisher, 459100; 1:2000); Core I/UQCRC1 (Life Technologies/Thermo Fisher, 459140; 1:2000); NDUFV1 (Abcam, ab55535; 1:1000); NDUFS8 (Abcam, ab170936; 1:1000); SDHAF2 (Cell Signaling, 45849; 1:1000); SDHAF4 (Thermo Fisher, PA5-73014; 1:1000; or Sigma, HPA031824; 1:500); FAD (MyBioSource, MBS2015613; 1:500); HRP-conjugated tubulin (Thermo Scientific, MA5-16308-HRP; 1:2000); HRP-conjugated actin (Abcam, ab49900; 1:5000); actin (Abcam, ab14715 or 3700, or Cell Signaling, 4970 or 3700; all 1:3000); DHODH (Proteintech, 14877-1-AP; 1:500); CAD (Cell Signaling, 93925; 1:1000); phospho-Histone H3 (Ser10) (Cell Signaling, 3642; 1:1000); GAPDH (Cell Signaling, 8337; 1:3000). Uncropped western blots are in Supplementary Fig. 8.

Isolation of mitochondria and NBGE. Mitochondria were isolated using Dounce or Balch homogenizers, followed by standard differential centrifugation^{13,50,70}. Experimental procedure and antibodies for NBGE were used as described previously^{57,71}. In brief, digitonin-solubilised mitochondria were separated on NativePAGE Novex Bis-Tris 3–12% gradient gels. After electrophoresis, the gels were incubated in transfer buffer containing 0.1% SDS for 10 min and proteins were transferred to PVDF membranes probed with specific antibodies (all diluted 1:500, except for VDAC1 and HSP60 diluted 1:1000) against complex I (NDUFA9, ab14713, Abcam; or NDUFB8, ab110242, Abcam), CII (*SDHA*, 14715, Abcam), CIII (Core2, ab14745, Abcam), CIV (COXVa, ab110262, Abcam) and CV (ATP5A, ab14748, Abcam; or ATP5B, HPA001520, Sigma Aldrich), and VDAC1 (ab15895, Abcam) or HSP60 (12165S, Cell Signaling) as the loading control.

Evaluation of oxygen consumption rate. Cells were seeded into an XFp assay microplate (Agilent) 1 day prior to evaluation. On the day of the assay, the growth medium was replaced with the XF assay medium (Agilent) supplemented with glucose and glutamine. Oxygen consumption rate (OCR) measurements were made using the Seahorse Analyzer (Agilent) with sequential addition of oligomycin, FCCP, rotenone and antimycin A (using the Mitostress kit from Agilent) according to the manufacturer's protocol. OCR measurements were adjusted based on the cell number counted at the end of the experiment.

Respiration assays. Respiration was evaluated in digitonin-permeabilized MDA231 sublines and assessed as described previously^{72,73}. In brief, the cells were trypsinized, washed with PBS, re-suspended at 1 × 10⁶ cells per ml of the Mir05 medium (0.5 mM EGTA, 3 mM MgCl₂, 60 mM K-lactobionate, 20 mM taurine, 10 mM KH₂PO₄, 110 mM sucrose, 1 g/l essentially fatty acid-free bovine serum albumin, 20 mM Hepes, pH 7.1 at 30 °C) and transferred to the chamber of the Oxygraph-2k instrument (Oroboros). Respiration measurements were performed at 37 °C. Cells were permeabilized with 5 µg digitonin per 10⁶ cells, followed by sequential additions of substrate and inhibitors. CI respiration was assessed in the presence of glutamate/malate and ADP, while CII respiration in the presence of succinate, ADP, and rotenone.

Xenograft experiments. All procedures with animals were performed according to the Institutional guidelines and ethical authorization by the Griffith University Animal Ethics Committee. MDA231 sublines were injected into the mammary fat pad of Balb-c nu/nu mice at 10^6 cells per animal. Tumor volume was quantified using the Vevo3100 USI system using a 30- μ m resolution scan-head^{70,74}.

SWATH proteomic analysis. For proteomic analysis, cell pellets were lysed using 200 μ l of sodium deoxycholate buffer (0.1% in 0.1 M triethyl ammonium bicarbonate). Following reduction with 5 mM dithiothreitol and alkylation with 10 mM iodoacetamide, 100 μ g of protein was digested with sequencing grade trypsin (Promega) at 37 °C for 16 h. The sample was acidified using formic acid and centrifuged for 10 min to remove the precipitated sodium deoxycholate salt. Tryptic peptides were recovered and fractionated using High pH Reversed-Phase Peptide Fractionation Kit (Pierce) according to manufacturer's instructions, with the exception that only six fractions were collected. To establish a reference spectral library for SWATH analysis, the fractionated sample was run by nanoLC-MS/MS using a 100 mm \times 150 μ m C18 column coupled to an Eksigent Ultra system over 90 min as described⁷⁵ using Information-Dependent Acquisition (IDA) on a 5600 + Triple TOF mass spectrometer (Sciex, Framingham, MA) using the Top 10 most intense multiply charged ions. MS/MS was conducted for 50 ms over the 100–1500 m/z range. Peptides were identified using ProteinPilot (v4.2) (Sciex) to search the UniProt Human protein database (20,198 entries, downloaded June 2015) and false-discovery controlled by searching a reversed-decoy Human database of identical size, selecting >99% confidence for protein identification. The Paragon group file was imported into PeakView software 2.1 using the SWATH MicroApp 2.0 to generate a sample specific spectral library.

For SWATH data acquisition of individual samples, we used the same MS setup but adjusted the method to use 60 variable m/z windows (400–1250 m/z) for precursor ion selection. The MS/MS spectra were accumulated for 60 ms in the m/z 350–1500 m/z range.

To extract SWATH peak areas with PeakView software 2.1, we carried out retention time calibration with endogenous peptides and data processing using following settings; 100 maximal peptides per protein, maximal 6 transitions per peptide, peptide confidence threshold of 99%, transition false discovery rate <1%, 10 min extraction window, and fragment extraction tolerance of 75 ppm, exclusion of shared peptides. The protein peak areas were normalized to the total peak area and log-transformed peak areas and subjected to Student's *t*-test to compare relative protein peak area between samples. Proteins were considered to be differentially expressed with $p < 0.05$ and protein fold change was ± 1.5 fold. DAVID⁷⁶ was used for functional enrichment analysis. The Benjamini method (adjusted p value) was used to control the family-wide false discovery rate for enrichment analysis.

Identification of SDHA-interacting proteins. Mitochondria isolated from SDHB^{KO} cell stably expressing SDHA-FLAG and empty vector were lysed using membrane solubilization buffer (1% *n*-dodecyl β -D-maltoside, 20 mM Tris-HCl, pH 7.4, 0.1 mM EDTA, 100 mM NaCl, 10% glycerol) supplemented with protease inhibitors (Roche). Protein concentrations were determined using the BCA protein assay kit. Equal amounts of protein were incubated with 20 μ l anti-FLAG M2 agarose beads (Sigma) overnight at 4 °C. Beads were washed three times with the membrane solubilization buffer. The proteins bound to the beads were then eluted with 2 \times SDS lysis buffer and separated by 15% SDS-PAGE followed by silver staining (Mass spectrometry compatible, Life Technologies). Protein bands from control and treatment lanes were subjected to tryptic digest and analyzed by mass spectrometry.

Sample preparation for NMR spectroscopy and LC-MS. Metabolites were extracted from parental, SDHB^{KO}EV, and SDHB^{KO}SDHA^{low} cells (3×10^6 cells) with 400 μ l of mixture composed of methanol, acetonitrile, and distilled water (5:3:2). The samples were centrifuged at 15,000 \times g for 20 min at 4 °C. The supernatant was collected, divided into two portions at the ratio of 1:5 for LC-MS and NMR analysis, and dried with a vacuum centrifuge (Vision). The pellets for LC-MS were dissolved with 30 μ l mixture of HPLC-grade acetonitrile and water (1:1), and those for NMR with 500 μ l buffer composed of 2 mM Na₂HPO₄ and 5 mM NaH₂PO₄ in D₂O with 0.025% TSP (trimethylsilylpropionic acid sodium salt-D₄) as an internal standard. For the isotopologue distribution analysis, these cells were cultured in glucose and glutamine-free DMEM media (Gibco) supplemented with 10% dialyzed FBS (Welgene, Daegu, Korea), 10% D₂O, 5 mM unlabeled glucose, and 20 mM U-¹³C₆-labeled glucose (Cambridge Isotope Laboratories) or 4 mM U-¹³C₅-labeled glutamine (Cambridge Isotope Laboratories) for 24 h before metabolites extraction, respectively.

Measurement and analysis for NMR spectroscopy and LC-MS. Untargeted metabolomic profiling was performed using NMR, and targeted profiling by LC-MS multiple reaction monitoring for metabolites that are not readily discernible by NMR. Metabolites detected by both methods, such as succinate and glutamate, exhibited consistent results. 1D NMR spectra were obtained using a 500-MHz Bruker Avance spectrometer equipped with a cryogenic triple resonance probe (KBISI). For the pulse program, 'noesygppr1d' was used with 64 scans, and the final

spectra were constructed to 16K points. The metabolites were identified with Chenomx spectral database (Edmonton, Alberta, Canada) and comparison with standard compounds³⁹. LC-MS data were obtained with an LTQ XL high performance linear ion trap mass spectrometer (Thermo Fisher Scientific) equipped with an electrospray ionization source. The operating conditions of the mass spectrometer were as follows: 5 kV of ion spray voltage, heated capillary temperature of 275 °C, and sheath gas (nitrogen), auxiliary gas (nitrogen), and sweep gas (nitrogen) pressures of 35, 10, and 2 (arbitrary units), respectively. Full scanning analyses were performed in the range of m/z 85–1000, and a 35-V normalized collision energy was used for MS/MS. Mobile phases were 10 mM ammonium carbonate (pH 9.1) in distilled water (A) and acetonitrile (B), and the flowrate was 0.15 ml/min. The gradient scheme was as follows: 80% B at 0 min, 35% B at 10 min, 5% B at 12 min, 5% B at 25 min, 80% B at 25.1 min, and 80% B at 35 min. The Zic-Hilic Polymeric Beads Peek Column (150 \times 2.1 mm, 5 μ m; Merck) was used at 35 °C, and the autosampler temperature was set at 4 °C. The peak areas of parental ion and its isotopologues were measured using Xcalibur (Thermo Fisher Scientific). The metabolites were identified by m/z values and MS/MS fragmentation patterns from Human Metabolome Database (HMDB) and METLIN databases and also by comparison with standard compounds⁷⁷. For multivariate analysis, the NMR data were Fourier-transformed, phase-corrected, and baseline-corrected manually using MestReNova (Mestrelab Research, Santiago de Compostela, Spain). The signal intensities were normalized against the intensity of the 0.025% TSP signal at 0 ppm and total area values. The processed NMR data were saved into a text file and binned at a 0.004-ppm interval. The water region (4.66–5.0) was excluded from the spectra. The binning and normalization were performed using a Perl software written in-house⁷⁸. The region corresponding to water (4.66–5.0 ppm) was removed from the spectra, and the data were imported into SIMCA-P software (Umetrics) for PLS-DA. The heat map was constructed with a relative Z-score of peak area of each metabolite identified by NMR and LC-MS.

RNA sequence analysis. RNA was isolated using RNAzol (Molecular Research Center) according to the manufacturer's instructions. RNA was dissolved in the TE buffer (ThermoFisher), and remaining DNA contamination was removed using DNase I (Sigma-Aldrich) for 30 min. To clean RNA, the same volume of 8 M LiCl (Sigma-Aldrich) was added and incubated overnight at –20 °C. Samples were centrifuged for 30 min at 16,100 \times g/2 °C; the supernatant was removed and the pellet washed twice in 80% ethanol, followed by centrifugation as above. The remaining ethanol was evaporated at 65 °C for 10 min, and RNA was dissolved in 20 μ l of TE buffer. Total RNA concentration was measured by Nanodrop 2000, and its quality was assessed by the Fragment Analyzer (Advanced Analytical) using Standard Sensitivity RNA Analysis Kit (Advanced Analytical). The libraries were prepared from 2 μ g of total RNA using QuantSeq 3'mRNA-Seq Library Prep Kit FWD for Illumina (Lexogen), pooled and sequenced on MiSeq v3 kit in the 150 bp SE mode.

About 2 million reads per sample were obtained, and low-quality reads were filtered out using TrimmomaticSE (v. 0.36⁷⁹) with parameters "trimmomatic/TRIM_MDA_K4_1_sequence.fastq CROP:165 HEADCROP:12 ILLUMINACLIP:~/Lexogen_quantseq.fa:2:30:10 LEADING:3 TRAILING:3 SLIDINGWINDOW:4:15 MINLEN:36". Ribosomal and mitochondrial RNA reads were removed using Sortmerna (v 2.1b⁸⁰) using default parameters. The remaining reads were aligned to the Human Genome Version GRCh38.87 and count tables were generated using STAR (v 2.5.2b^{81,82}). Differentially expressed genes (DEGs) were analyzed by means of DESeq2 (v 1.18.0⁸²) using the default function "DESeq" without altered parameters. Result tables were generated as contrast between the SDHB^{KO} and parental, SDHB^{KO}SDHA^{low} and parental, and SDHB^{KO} and SDHB^{KO}SDHA^{low} cells. Genes with padj <0.1 for at least one pair of comparisons were chosen as DEGs. The function "plotPCA" from DESeq2 package with default parameters was used for PCA analysis. The heat-map was created from rlog transformed count data after subtraction of their mean values for every DEG. Altogether, we identified 523 significantly changed genes out of the total number of 7587 detected genes (DESeq2 BaseMean >5). The data have been deposited in NCBI's Gene Expression Omnibus and are accessible through GEO Series accession number GSE108938.

For gene set enrichment analysis, DEGs were filtered and used for clustering and ontology analysis. The normalized counts of these genes for all biological replicates and cell lines (parental-MDA231, SDHB^{KO}-SHB, and SDHB^{KO}SDHA^{low}-SH1) were used to analyze for patterns of expression across the three cell lines. The data were first normalized across cell lines by dividing the mean of the replicates by the sum of the mean of the replicates. The R package optCluster (R ver. 3.4.3) was then used to determine the best clustering algorithm among agnes, clara, diana, hierarchical, kmeans, pam, and sota clustering methods using the validation methods connectivity, Dunn index and silhouette width, and the number of clusters set to ten⁸³. Clusters that showed similar expression profiles were then merged.

Gene ontology was performed on the genes from each unique cluster, using the R package gprofiler, to identify significantly (p -value < 0.05) enriched GO terms⁸⁴. The genes were analyzed with no specified ranking while the gSCS (Set Counts and Sizes) algorithm was used to determine the significance threshold. All identified genes from the RNASeq were used as background. GO annotations inferred by in silico methods were included in the analysis.

After the genes were linked to their appropriate GO terms, REVIGO was used to cluster similar GO terms together while using the *p*-value output from gprofiler to create a ranked list⁸⁵. A similarity of 0.7 using the SimRel semantic similarity method was used to group similar GO terms and the UniProt database (15 March 2017) was used to find the relevant GO term sizes. Output from REVIGO was visualized as treemaps.

2D in-cell NMR analysis. Six plates of 70% confluent cultured cells were harvested with centrifugation. After re-suspending the cells with 5 ml DPBS, the cells were counted and 3×10^7 cells were transferred into a fresh tube. After centrifugation, the harvested cells were re-suspended in 500 μ l glucose-free DMEM media (Gibco) supplemented with 10% dialyzed FBS, 25 mM U-¹³C₆-labeled glucose, and 10% D₂O. The cells were spun in an NMR (30 g, 100 s) to allow sedimentation, enough to cover the active region of the NMR detection coil. ¹H-¹³C Heteronuclear Single Quantum Coherence (HSQC) NMR spectra were measured using the 800-MHz Bruker Avance spectrometer equipped with a cryogenic triple resonance probe (Seoul National University). The dataset comprises 1024 \times 128 points for direct and indirect dimensions, respectively. The time course spectral measurement was obtained at 310 K for 24 time points, with each experiment lasting for 288 s (13 points). Each metabolite was identified by spiking the standard compound.

Transmission electron microscopy. TEM was accomplished as follows. Cells were grown on cover-slips, fixed with 2% glutaraldehyde (Agar Scientific) and post-fixed with 1% OsO₄ made up in Sorensen's phosphate buffer (0.1 M, pH 7.2–7.4), dehydrated, and embedded in Epon-Durkupan (Sigma-Aldrich). Ultrathin sections (~70–90 nm) were cut, contrasted with uranyl acetate (Agar Scientific), and examined in the Morgagni 268 transmission electron microscope (FEI) at 80 kV and in the TECNAI G2 20 LaB6 electron microscope (FEI) at 200 kV. Images were captured with Mega View III CCD camera (Olympus Soft Imaging Solutions).

Paranglioma patients. Tumor tissue from 6 patients (3 with *SDHB* mutations, 1 with *SDHA* mutation, 2 sporadic) was used in this study. Tumor tissue was obtained during surgery at the National Institutes of Health (NIH). Genetic testing was performed by NIH in collaboration with the Mayo Clinic (Rochester, MN, USA) or the results were sent from external facilities to the NIH. Expression of *SDHB* and *SDHA* proteins was also evaluated by immunohistochemistry as previously described⁸⁶. Signed written consent was obtained from all patients prior to any experimental work. The use of patient samples was allowed by the Eunice Kennedy Shriver NICHD IRB (Ethics Approval #00-CH-0093). The tumor samples examined were as follows (Sample code, affected subunit, DNA base pair change, protein amino acid change): S/ne7, *SDHB*, c.183T>G, p.Tyr61X; S-275, *SDHB*, c.526G>T, p.Glu17X; S-73, *SDHB*, c.268C>T, p.Arg90X; S-281 A/B, *SDHA*, c.91C>T, p.Arg31X; S-187, Sporadic, no CII subunit affected; S-76, Sporadic, no CII subunit affected.

Statistical evaluation. Unless stated otherwise, data are mean values \pm SD of at least three independent experiments. In mouse experiments, groups of 6 animals were used, unless stated otherwise. The two-tailed unpaired Student's *t*-test was used to assess statistical significance with *p* < 0.05 being regarded as significant. Images are representative of three independent experiments.

Data availability. RNA sequence data are filed in NCBI's Gene Expression Omnibus and are accessible through GEO Series accession number GSE108938. The mass spectrometry proteomics data have been deposited to the ProteomeXchange Consortium via the PRIDE partner repository with the dataset identifier PXD009656. All other data that support findings of this study are available from the corresponding authors upon request.

Received: 3 September 2017 Accepted: 7 May 2018

Published online: 07 June 2018

References

- Jones, R. G. & Thompson, C. B. Tumor suppressors and cell metabolism: a recipe for cancer growth. *Genes Dev.* **23**, 537–548 (2009).
- King, A., Selak, M. A. & Gottlieb, E. Succinate dehydrogenase and fumarate hydratase: linking mitochondrial dysfunction and cancer. *Oncogene* **25**, 4675–4682 (2006).
- Selak, M. A. et al. Succinate links TCA cycle dysfunction to oncogenesis by inhibiting HIF- α prolyl hydroxylase. *Cancer Cell* **7**, 77–85 (2005).
- Bezawork-Geleta, A., Rohlena, J., Dong, L., Pacak, K. & Neuzil, J. Mitochondrial Complex II: at the Crossroads. *Trends Biochem. Sci.* **42**, 312–325 (2017).
- Fendt, L. et al. Accumulation of mutations over the entire mitochondrial genome of breast cancer cells obtained by tissue microdissection. *Breast Cancer Res. Treat.* **128**, 327–336 (2011).
- Parrella, P. et al. Detection of mitochondrial DNA mutations in primary breast cancer and fine-needle aspirates. *Cancer Res.* **61**, 7623–7626 (2001).
- Tseng, L. M. et al. Mitochondrial DNA mutations and mitochondrial DNA depletion in breast cancer. *Genes Chromosomes Cancer* **45**, 629–638 (2006).
- Wallace, D. C. Mitochondria and cancer. *Nat. Rev. Cancer* **12**, 685–698 (2012).
- McKenzie, M., Lazarou, M., Thorburn, D. R. & Ryan, M. T. Mitochondrial respiratory chain supercomplexes are destabilized in Barth Syndrome patients. *J. Mol. Biol.* **361**, 462–469 (2006).
- Lapuente-Brun, E. et al. Supercomplex assembly determines electron flux in the mitochondrial electron transport chain. *Science* **340**, 1567–1570 (2013).
- Acin-Perez, R., Fernandez-Silva, P., Peleato, M. L., Perez-Martos, A. & Enriquez, J. A. Respiratory active mitochondrial supercomplexes. *Mol. Cell* **32**, 529–539 (2008).
- Kovarova, N. et al. High molecular weight forms of mammalian respiratory chain complex II. *PLoS ONE* **8**, e71869 (2013).
- Tan, A. S. et al. Mitochondrial genome acquisition restores respiratory function and tumorigenic potential of cancer cells without mitochondrial DNA. *Cell Metab.* **21**, 81–94 (2015).
- Plass, C. et al. Mutations in regulators of the epigenome and their connections to global chromatin patterns in cancer. *Nat. Rev. Genet.* **14**, 765–780 (2013).
- Maiuri, M. C. & Kroemer, G. Essential role for oxidative phosphorylation in cancer progression. *Cell Metab.* **21**, 11–12 (2015).
- Leach, K. L. et al. The site of action of oxazolidinone antibiotics in living bacteria and in human mitochondria. *Mol. Cell* **26**, 393–402 (2007).
- Prezant, T. R. et al. Mitochondrial ribosomal RNA mutation associated with both antibiotic-induced and non-syndromic deafness. *Nat. Genet.* **4**, 289–294 (1993).
- Ramachandran, A. et al. Inhibition of mitochondrial protein synthesis results in increased endothelial cell susceptibility to nitric oxide-induced apoptosis. *Proc. Natl Acad. Sci. USA* **99**, 6643–6648 (2002).
- Maio, N. et al. Disease-causing SDHAF1 mutations impair transfer of Fe-S clusters to SDHB. *Cell Metab.* **23**, 292–302 (2016).
- van Nederveen, F. H. et al. An immunohistochemical procedure to detect patients with paraganglioma and pheochromocytoma with germline *SDHB*, *SDHC*, or *SDHD* gene mutations: a retrospective and prospective analysis. *Lancet Oncol.* **10**, 764–771 (2009).
- Bezawork-Geleta, A., Saiyed, T., Dougan, D. A. & Truscott, K. N. Mitochondrial matrix proteostasis is linked to hereditary paraganglioma: LON-mediated turnover of the human flavinylation factor SDH5 is regulated by its interaction with SDHA. *FASEB J.* **28**, 1794–1804 (2014).
- Sun, F. et al. Crystal structure of mitochondrial respiratory membrane protein complex II. *Cell* **121**, 1043–1057 (2005).
- Robinson, B. H., Petrova-Benedict, R., Buncic, J. R. & Wallace, D. C. Nonviability of cells with oxidative defects in galactose medium: a screening test for affected patient fibroblasts. *Biochem. Med. Metab. Biol.* **48**, 122–126 (1992).
- Benard, G. & Rossignol, R. Ultrastructure of the mitochondrion and its bearing on function and bioenergetics. *Antioxid. Redox Signal.* **10**, 1313–1342 (2008).
- Stroud, D. A., Formosa, L. E., Wijeyeratne, X. W., Nguyen, T. N. & Ryan, M. T. Gene knockout using transcription activator-like effector nucleases (TALENs) reveals that human NDUFA9 protein is essential for stabilizing the junction between membrane and matrix arms of complex I. *J. Biol. Chem.* **288**, 1685–1690 (2013).
- Oostveen, F. G., Au, H. C., Meijer, P. J. & Scheffler, I. E. A Chinese hamster mutant cell line with a defect in the integral membrane protein CII-3 of complex II of the mitochondrial electron transport chain. *J. Biol. Chem.* **270**, 26104–26108 (1995).
- Housley, S. L. et al. Renal carcinoma with giant mitochondria associated with germ-line mutation and somatic loss of the succinate dehydrogenase B gene. *Histopathology* **56**, 405–408 (2010).
- Rost, H. L. et al. OpenSWATH enables automated, targeted analysis of data-independent acquisition MS data. *Nat. Biotechnol.* **32**, 219–223 (2014).
- Ghazalpour, A. et al. Comparative analysis of proteome and transcriptome variation in mouse. *PLoS Genet.* **7**, e1001393 (2011).
- Huang, S. et al. Complementary iTRAQ proteomics and RNA-seq transcriptomics reveal multiple levels of regulation in response to nitrogen starvation in *Synechocystis* sp. PCC 6803. *Mol. Biosyst.* **9**, 2565–2574 (2013).
- Cenik, C. et al. Integrative analysis of RNA, translation, and protein levels reveals distinct regulatory variation across humans. *Genome Res.* **25**, 1610–1621 (2015).
- Liu, Y., Beyer, A. & Aebersold, R. On the dependency of cellular protein levels on mRNA abundance. *Cell* **165**, 535–550 (2016).
- Bauernfeind, A. L. & Babbitt, C. C. The predictive nature of transcript expression levels on protein expression in adult human brain. *BMC Genomics* **18**, 322 (2017).
- Mitchell, A. D. & Hoogenraad, N. J. De novo pyrimidine nucleotide biosynthesis in synchronized rat hepatoma (HTC) cells and mouse embryo fibroblast (3T3) cells. *Exp. Cell Res.* **93**, 105–110 (1975).

35. Sigoillot, F. D., Berkowski, J. A., Sigoillot, S. M., Kotsis, D. H. & Guy, H. I. Cell cycle-dependent regulation of pyrimidine biosynthesis. *J. Biol. Chem.* **278**, 3403–3409 (2003).
36. Lane, A. N. & Fan, T. W. Regulation of mammalian nucleotide metabolism and biosynthesis. *Nucleic Acids Res.* **43**, 2466–2485 (2015).
37. Vander Heiden, M. G., Cantley, L. C. & Thompson, C. B. Understanding the Warburg effect: the metabolic requirements of cell proliferation. *Science* **324**, 1029–1033 (2009).
38. Ackerman, D. & Simon, M. C. Hypoxia, lipids, and cancer: surviving the harsh tumor microenvironment. *Trends Cell Biol.* **24**, 472–478 (2014).
39. Wen, H., An, Y. J., Xu, W. J., Kang, K. W. & Park, S. Real-time monitoring of cancer cell metabolism and effects of an anticancer agent using 2D in-cell NMR spectroscopy. *Angew. Chem. Int. Ed. Engl.* **54**, 5374–5377 (2015).
40. Killian, J. K. et al. Succinate dehydrogenase mutation underlies global epigenomic divergence in gastrointestinal stromal tumor. *Cancer Discov.* **3**, 648–657 (2013).
41. Kitazawa, S. et al. Succinate dehydrogenase B-deficient cancer cells are highly sensitive to bromodomain and extra-terminal inhibitors. *Oncotarget* **8**, 28922–28938 (2017).
42. Letouze, E. et al. SDH mutations establish a hypermethylator phenotype in paraganglioma. *Cancer Cell* **23**, 739–752 (2013).
43. Lussey-Lepoutre, C. et al. Loss of succinate dehydrogenase activity results in dependency on pyruvate carboxylation for cellular anabolism. *Nat. Commun.* **6**, 8784 (2015).
44. Cardaci, S. et al. Pyruvate carboxylation enables growth of SDH-deficient cells by supporting aspartate biosynthesis. *Nat. Cell Biol.* **17**, 1317–1326 (2015).
45. DeBerardinis, R. J. & Chandel, N. S. Fundamentals of cancer metabolism. *Sci. Adv.* **2**, e1600200 (2016).
46. Boroughs, L. K. & DeBerardinis, R. J. Metabolic pathways promoting cancer cell survival and growth. *Nat. Cell Biol.* **17**, 351–359 (2015).
47. Yang, C. et al. Glutamine oxidation maintains the TCA cycle and cell survival during impaired mitochondrial pyruvate transport. *Mol. Cell* **56**, 414–424 (2014).
48. Mullen, A. R. et al. Reductive carboxylation supports growth in tumour cells with defective mitochondria. *Nature* **481**, 385–388 (2011).
49. Lendvai, N. et al. Succinate-to-fumarate ratio as a new metabolic marker to detect the presence of SDHB/D-related paraganglioma: initial experimental and ex vivo findings. *Endocrinology* **155**, 27–32 (2014).
50. Kluckova, K. et al. Ubiquinone-binding site mutagenesis reveals the role of mitochondrial complex II in cell death initiation. *Cell Death Dis.* **6**, e1749 (2015).
51. Cecchini, G. Function and structure of complex II of the respiratory chain. *Annu. Rev. Biochem.* **72**, 77–109 (2003).
52. Hao, H. X. et al. SDH5, a gene required for flavination of succinate dehydrogenase, is mutated in paraganglioma. *Science* **325**, 1139–1142 (2009).
53. Qi, W. et al. Pyruvate kinase M2 activation may protect against the progression of diabetic glomerular pathology and mitochondrial dysfunction. *Nat. Med.* **23**, 753–762 (2017).
54. Ye, J. et al. Pyruvate kinase M2 promotes de novo serine synthesis to sustain mTORC1 activity and cell proliferation. *Proc. Natl Acad. Sci. USA* **109**, 6904–6909 (2012).
55. Schulze, A. & Harris, A. L. How cancer metabolism is tuned for proliferation and vulnerable to disruption. *Nature* **491**, 364–373 (2012).
56. Christofk, H. R., Vander Heiden, M. G., Wu, N., Asara, J. M. & Cantley, L. C. Pyruvate kinase M2 is a phosphotyrosine-binding protein. *Nature* **452**, 181–186 (2008).
57. Bezawork-Geleta, A., Dong, L., Rohlena, J. & Neuzil, J. The assembly factor SDHAF2 is dispensable for flavination of the catalytic subunit of mitochondrial complex II in breast cancer cells. *J. Biol. Chem.* **291**, 21414–21420 (2016).
58. Brown, K. K., Spinelli, J. B., Asara, J. M. & Toker, A. Adaptive reprogramming of De Novo pyrimidine synthesis is a metabolic vulnerability in triple-negative breast cancer. *Cancer Discov.* **7**, 391–399 (2017).
59. Mathur, D. et al. PTEN regulates glutamine flux to pyrimidine synthesis and sensitivity to dihydroorotate dehydrogenase inhibition. *Cancer Discov.* **7**, 380–390 (2017).
60. Rabinovich, S. et al. Diversion of aspartate in ASS1-deficient tumours fosters de novo pyrimidine synthesis. *Nature* **527**, 379–383 (2015).
61. Zong, H. et al. AMP kinase is required for mitochondrial biogenesis in skeletal muscle in response to chronic energy deprivation. *Proc. Natl Acad. Sci. USA* **99**, 15983–15987 (2002).
62. Hardie, D. G., Ross, F. A. & Hawley, S. A. AMPK: a nutrient and energy sensor that maintains energy homeostasis. *Nat. Rev. Mol. Cell Biol.* **13**, 251–262 (2012).
63. Canto, C. et al. AMPK regulates energy expenditure by modulating NAD⁺ metabolism and SIRT1 activity. *Nature* **458**, 1056–1060 (2009).
64. Guaras, A. et al. The CoQH2/CoQ ratio serves as a sensor of respiratory chain efficiency. *Cell Rep.* **15**, 197–209 (2016).
65. Benn, D. E. et al. Clinical presentation and penetrance of pheochromocytoma/paraganglioma syndromes. *J. Clin. Endocrinol. Metab.* **91**, 827–836 (2006).
66. Fishbein, L. et al. Comprehensive molecular characterization of pheochromocytoma and paraganglioma. *Cancer Cell* **31**, 181–193 (2017).
67. Jochmanova, I. & Pacak, K. Pheochromocytoma: the first metabolic endocrine cancer. *Clin. Cancer Res.* **22**, 5001–5011 (2016).
68. Sancak, Y. et al. EMRE is an essential component of the mitochondrial calcium uniporter complex. *Science* **342**, 1379–1382 (2013).
69. Blecha, J. et al. Antioxidant defense in quiescent cells determines selectivity of electron transport chain inhibition-induced cell death. *Free Radic. Biol. Med.* **112**, 253–266 (2017).
70. Rohlenova, K. et al. Selective disruption of respiratory supercomplexes as a new strategy to suppress Her2high breast cancer. *Antioxid. Redox Signal.* **26**, 84–103 (2017).
71. Vondrusova, M., Bezawork-Geleta, A., Sachhibulkij, K., Truksa, J. & Neuzil, J. The effect of mitochondrially targeted anticancer agents on mitochondrial (super)complexes. *Methods Mol. Biol.* **1265**, 195–208 (2015).
72. Pasdar, E. A. et al. Characterisation of mesothelioma-initiating cells and their susceptibility to anti-cancer agents. *PLoS ONE* **10**, e0119549 (2015).
73. Yan, B. et al. Mitochondrially targeted vitamin E succinate efficiently kills breast tumour-initiating cells in a complex II-dependent manner. *BMC Cancer* **15**, 401 (2015).
74. Dong, L. F. et al. Horizontal transfer of whole mitochondria restores tumorigenic potential in mitochondrial DNA-deficient cancer cells. *Elife* **6**, 1–22 (2017).
75. Wu, J. X. et al. SWATH mass spectrometry performance using extended peptide MS/MS assay libraries. *Mol. Cell. Proteom.* **15**, 2501–2514 (2016).
76. Huang da, W., Sherman, B. T. & Lempicki, R. A. Bioinformatics enrichment tools: paths toward the comprehensive functional analysis of large gene lists. *Nucleic Acids Res.* **37**, 1–13 (2009).
77. Wen, H. et al. Enhanced phase II detoxification contributes to beneficial effects of dietary restriction as revealed by multi-platform metabolomics studies. *Mol. Cell. Proteomics* **12**, 575–586 (2013).
78. Wen, H. et al. A new NMR-based metabolomics approach for the diagnosis of biliary tract cancer. *J. Hepatol.* **52**, 228–233 (2010).
79. Bolger, A. M., Lohse, M. & Usadel, B. Trimmomatic: a flexible trimmer for Illumina sequence data. *Bioinformatics* **30**, 2114–2120 (2014).
80. Kopylova, E., Noe, L. & Touzet, H. SortMeRNA: fast and accurate filtering of ribosomal RNAs in metatranscriptomic data. *Bioinformatics* **28**, 3211–3217 (2012).
81. Dobin, A. et al. STAR: ultrafast universal RNA-seq aligner. *Bioinformatics* **29**, 15–21 (2013).
82. Love, M. I., Huber, W. & Anders, S. Moderated estimation of fold change and dispersion for RNA-seq data with DESeq2. *Genome Biol.* **15**, 550 (2014).
83. Sekula, M., Datta, S. & Datta, S. optCluster: an R Package for Determining the Optimal Clustering Algorithm. *Bioinformatics* **13**, 101–103 (2017).
84. Reimand, J. et al. g:Profiler—a web server for functional interpretation of gene lists (2016 update). *Nucleic Acids Res.* **44**, W83–W89 (2016).
85. Supek, F., Bosnjak, M., Skunca, N. & Smuc, T. REVIGO summarizes and visualizes long lists of gene ontology terms. *PLoS ONE* **6**, e21800 (2011).
86. Papatomas, T. G. et al. SDHB/SDHA immunohistochemistry in pheochromocytomas and paragangliomas: a multicenter interobserver variation analysis using virtual microscopy: a Multinational Study of the European Network for the Study of Adrenal Tumors (ENS@T). *Mod. Pathol.* **28**, 807–821 (2015).

Acknowledgements

The work was supported in part by the ARC Discovery grant, Czech Science Foundation (15-02203S) and Czech Health Foundation grant (17-30138A) to J.N., bilateral funding by the Czech Science Foundation and National Science Foundation of Korea (17-01192J/NRF-2016K2A9A1A06921853) to J.N. and S.P., Czech Science Foundation grant (17-20904S and 16-22823S) to J.R., funding by Genesis Oncology Trust, the Cancer Society of New Zealand and the Health Research Council of New Zealand to M.V.B., the Basic Science Research Program (2009-83533), the Bio-Synergy Research Project (NRF-2015M3A9C4075818) through the National Research Foundation of Korea funded by the Ministry of Education Science and Technology and Ministry of Science, ICT and Future Planning to S.P., by the Technology Agency of the Czech Republic (TE01020118) IMG grant (RVO: 68378050) to M.S. and P.H., and the institutional support of the Institute of Biotechnology RVO: 86652036, by the BIOCEV European Regional Development Fund CZ.1.05/1.1.00, and by the Intramural Research Program of the NIH, NICHD. H.W. was supported by the National Key Research and Development Program of China (2017YFA0503900) and Science and Technology Foundation of Shenzhen City (JCYJ20170302144650949). Proteomic analysis was facilitated by access to the Australian Proteomic Analysis Facility supported in part by the Australian Government's National Collaborative Research Infrastructure Strategy. The electron microscopy data were produced at the Microscopy Centre—Electron Microscopy Core Facility (Institute of Molecular Genetics, Czech Academy of Sciences, Prague, Czech Republic) supported by Ministry of Education, Youth and Sports of the Czech Republic (LM2015062 Czech-BioImaging).

Author contributions

A.B.-G. and J.N. conceived the project and designed the study. A.B.-G. performed the majority of the experiments. H.W. and S.P. designed and performed metabolomics study and analyzed the data. V.C., Y.P., and K.P. provided patient data and samples, and they performed H&E and ICH analysis. L.K., K.V., R.Z., S.M.N., and S.B. performed the respiration studies, WB, and SDHB re-expression. M.S. and P.H. performed TEM analysis. T.Z. and M.P.M. performed SWATH-MS and bioinformatics analysis. L.D., B.Y., J. V., J.R., S.Z., and M.V.B. contributed reagents, materials, analytical tools, technical support, and ideas. P.A., R.N., R.S., S.M.N., and M.K. performed RNA sequence analysis and interpreted the data. A.B.-G., J.R., and J.N. wrote the manuscript. All authors discussed the results and edited the manuscript.

Additional information

Supplementary Information accompanies this paper at <https://doi.org/10.1038/s41467-018-04603-z>.

Competing interests: The authors declare no competing interests.

Reprints and permission information is available online at <http://npg.nature.com/reprintsandpermissions/>

Publisher's note: Springer Nature remains neutral with regard to jurisdictional claims in published maps and institutional affiliations.



Open Access This article is licensed under a Creative Commons Attribution 4.0 International License, which permits use, sharing, adaptation, distribution and reproduction in any medium or format, as long as you give appropriate credit to the original author(s) and the source, provide a link to the Creative Commons license, and indicate if changes were made. The images or other third party material in this article are included in the article's Creative Commons license, unless indicated otherwise in a credit line to the material. If material is not included in the article's Creative Commons license and your intended use is not permitted by statutory regulation or exceeds the permitted use, you will need to obtain permission directly from the copyright holder. To view a copy of this license, visit <http://creativecommons.org/licenses/by/4.0/>.

© The Author(s) 2018